**RESEARCH ARTICLE**

**Open Access**

# Washover deposits related to tsunami and storm surge along the north coast of the Shimokita Peninsula in northern Japan

Daisuke Ishimura[1*] , Takashi Ishizawa[2], Masaki Yamada[3], Kaori Aoki[4] and Kai Sato[5]

## Abstract

A decade after the 2011 Tohoku-oki earthquake (Mw 9.0), geological surveys were conducted at multiple sites along the Pacific Coast of the tsunami-inundated Tohoku region in Japan, providing thousands of years of tsunami history. However, the challenges of correlation between historical records and geological tsunami deposits and identifying sources of historical and paleotsunamis have newly surfaced. Particularly the simultaneity and source of the 1611 Keicho tsunami in the Tohoku region and the seventeenth-century tsunami in the Hokkaido region are problematic. To solve such major issues, we conducted a tsunami-deposit survey at Sekinehama on the north coast of Shimokita Peninsula, near the junction of the Japan and Kuril trenches. We performed nondestructive analyses (X-ray computed tomography and micro-X-ray-fluorescence core scanning), grain-size analysis, tephra analysis, and radiocarbon dating of sediments from two coastal outcrops and inland drill cores. We identified five tsunami deposits (TD1–TD5) during the last 6 kyr and correlated them at a 200–400 m distance from the coast. They also correlate with previously identified tsunami deposits around the Shimokita Peninsula. From our study on tsunami deposits, we found other washover deposits in the coastal outcrops that are not represented in the inland cores. These indicate minor washover events related to small tsunamis and infrequent storm surges. The modeled age of the latest tsunami deposit is 500–300 cal yr BP (1450–1650 cal CE). This either correlates with two known tsunamis (the 1611 Keicho tsunami and another seventeenth-century tsunami) or is a previously unknown tsunami that occurred in the fifteenth–seventeenth centuries. If the latest tsunami deposit is to be accurately correlated with tsunami deposits previously identified within a 50-km distance from the study site, we need to consider an unknown fifteenth-century tsunami. Our investigation yields insights regarding the tsunami source in the vicinity of the junction of the Japan and Kuril trenches.

**Keywords:** Washover deposits, Tsunami, Storm surge, Shimokita Peninsula, B-Tm, To-Cu, ITRAX

## 1 Introduction

In the 10 years since the 2011 Tohoku-oki earthquake (Mw 9.0), tsunami-deposit research has shown dramatic progress not only in Japan but also across the world (Goto et al. 2014, 2021; Costa and Andrade 2020; Sawai 2020; Sugawara 2021). In addition to the discovery of new tsunami deposits, research on numerical modeling of tsunami and sediment transport (Sugawara 2021) and on tsunami size estimation (Namegaya and Satake 2014; Ishimura and Yamada 2019; Naruse and Abe 2017; Mitra et al. 2020, 2021) has been conducted. In particular, geological surveys were performed at multiple sites along the Pacific Coast of the Tohoku region where the 2011 tsunami inundated provided thousands of years of tsunami history (e.g., Goto et al. 2015; Ishimura and Miyauchi 2015, 2017; Takada et al. 2016; Inoue et al. 2017). Although long-term tsunami-deposit history was

*Correspondence: ishimura@tmu.ac.jp

[1] Department of Geography, Tokyo Metropolitan University, 1-1 Minami-Osawa, Hachioji, Tokyo 192-0397, Japan
Full list of author information is available at the end of the article

obtained at multiple sites, correlation between tsunami deposits from site to site and between historical records and geological surveys and estimation of the probable sources of historical and paleotsunamis have been challenging (Takashimizu 2014; Goto et al. 2021; Ishizawa et al. 2022).

Particularly for the fifteenth–seventeenth-century tsunami deposits whose ages cannot be sufficiently constrained by radiocarbon dating owing to wiggles in the calibration curve, the identification of the 1611 Keicho (e.g., Ebina and Imai 2014) and the 1454 Kyotoku (Namegaya and Yata 2014) tsunami deposits and the simultaneity and source of the 1611 Keicho tsunami in the Tohoku region and the seventeenth-century tsunami in the Hokkaido region remain major foci for investigation. Ishizawa et al. (2022) tackled the long-standing challenge of distinguishing the 1611 Keicho and 1454 Kyotoku tsunami deposits by applying high-resolution radiocarbon dating and concluded that only the 1611 Keicho tsunami deposit is distributed along the northern Sanriku Coast (Fig. 1a). Takashimizu (2014) discussed the simultaneity and wave source of the seventeenth-century tsunami in Hokkaido and the 1611 Keicho tsunami in Tohoku and the distribution and age of tsunami deposits in western Hokkaido, such as along the Hidaka Coast (Fig. 1a), to determine how widely distributed the seventeenth-century tsunami deposits are in Hokkaido. The northern part of the Pacific Coast of the Tohoku region, such as the Shimokita Peninsula, has high coastal dunes that limit appropriate sites for tsunami-deposit surveys in the north of Hachinohe (Fig. 1a, b) (Minoura et al. 2013; Tanigawa et al. 2014).

In our study, we conducted a tsunami-deposit survey at Sekinehama on the north coast of the Shimokita Peninsula in the northernmost part of the Pacific Coast of the Tohoku region (Fig. 1) to provide continuous and long-term tsunami history and fill in blank areas of tsunami-deposit information near the junction of the Japan and Kuril trenches. The multiple event deposits that we identified in the Holocene sediments and dated as from 6 ka or later are considered to be transported by tsunamis and storm surges. This study is in coordination with Sato et al. (in press in this special issue), who investigated the wave source of the latest tsunami deposit discussed in our study.

## 2  Settings

The geologic units along the north coast of the Shimokita Peninsula (Fig. 1b, c) consist of the Pliocene Sunagomata Formation, the Pleistocene Tanabu Formation, and superposed marine-terrace deposits of multiple ages within the Pleistocene (Tsushima and Takizawa 1977). Marine Isotope Stage 5e marine terraces are distributed across the study area (Fig. 1c) (Koike and Machida 2001),

and Holocene sediments are distributed in the lowlands and incised valleys. Tephra and drift pumice layers were already identified in the Holocene sediments at two outcrops along the coast (SKN-E and SKN-W in Fig. 1c). In SKN-W, Kobayashi (2019) found fallout ash of B-Tm tephra (946 CE; Oppenheimer et al. 2017) from Changbaishan. In SKN-E, fallout ash of To-Cu tephra (5986–5899 cal yr BP; Mclean et al. 2018) from Towada volcano was identified by Ishimura and Hiramine (2020), and drift pumice of To-Cu and U-2 tephras (5681–5619 cal yr BP; Mclean et al., 2018) from Ulleung Island, Korea, was identified by Hiramine et al. (in press).

Historical and observational records of tsunamis hitting this region (Table 1) show that they are of two types: seismic and volcanic tsunamis. Most of the seismic tsunamis in Hokkaido and Tohoku regions have their sources along the Pacific Coast. Records show that past tsunamis were < 3 m high and may not have inundated inland in the study area because the topographic height behind the present-day beach is 4–5 m (Fig. 1c). The recorded tsunami height of the 2011 Tohoku-oki earthquake 200 m west of the study site was 2.2–2.7 m (Mori et al. 2012), suggesting the absence of a large inundation of inland area in Sekinehama. Volcanic tsunamis are thought to be generated by sector collapses of volcanoes due to volcanic activity at Komagatake and Oshima-Oshima volcanoes in Hokkaido (Fig. 1a) (Nishimura and Miyaji 1998; Satake 2007). The tsunamis' inundation heights were documented and estimated near their source areas (Nishimura and Miyaji 1998; Satake 2007), but no such information is of record for on the Shimokita Peninsula.

Based on prior research or observational records, the following summarizes information known or proposed about widely recognized tsunami deposits along the Pacific Coast in the Hokkaido and Tohoku regions. The 1611 Keicho tsunami deposits have been identified from the Sendai Plain to the northern Sanriku Coast (e.g., Sawai et al. 2012; Ishimura and Miyauchi 2015; Takada et al. 2016; Ishizawa et al. 2022). The highest tsunami run-up height along the Sanriku Coast was estimated to be more than 25 m (Ebina and Imai 2014; Ishimura and Ebina 2021). Recently, using high-resolution radiocarbon dating, Ishizawa et al. (2022) confirmed that 1611 Keicho tsunami deposits are distributed along the northern Sanriku Coast (Fig. 1a). The seventeenth-century tsunami deposits are widely recognized in eastern Hokkaido (e.g., Nanayama et al. 2003; Sawai et al. 2009; Ishizawa et al. 2017). Tsunami source models for the seventeenth-century tsunami were proposed by Nanayama et al. (2003), Satake et al. (2008), and Ioki and Tanioka (2016). The latest model proposed by Ioki and Tanioka (2016) setting the fault off eastern Hokkaido calculated the total seismic moment magnitude as Mw 8.8. The simultaneity of this
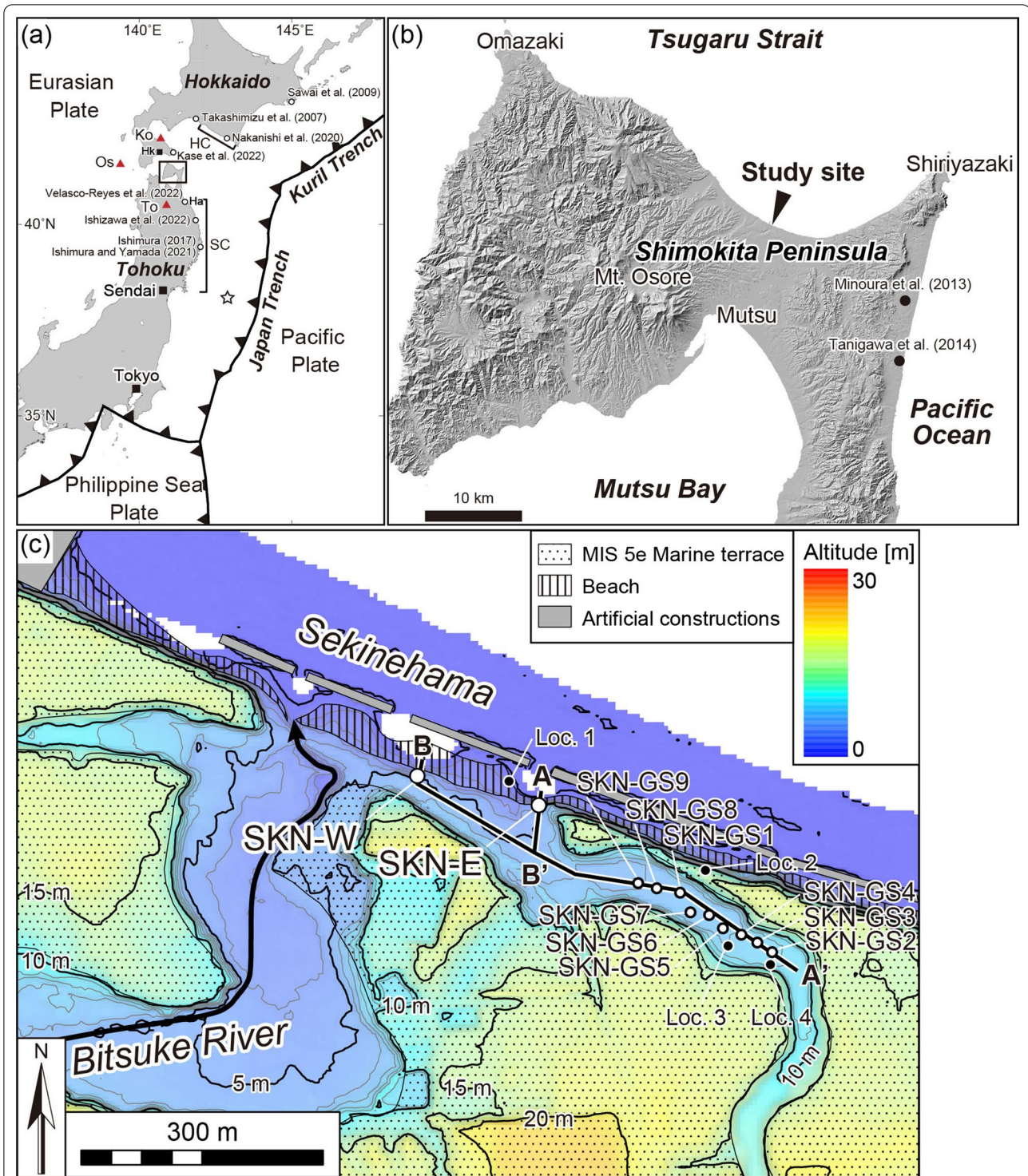
**Fig. 1** Study site. **a** Location of the Shimokita Peninsula. Ha: Hachinohe. Hk: Hakodate. Ko: Komagatake volcano. Os: Oshima-Oshima volcano. To: Towada volcano. SC: Sanriku Coast. HC: Hidaka Coast. Star denotes the epicenter of the 2011 Tohoku-oki earthquake. Rectangle indicates area represented by (**b**). **b** Northern Shimokita Peninsula. Shaded relief map is based on a 10-m-mesh digital elevation model (DEM) from the Geospatial Information Authority of Japan (GSI). **c** Map of the Sekinehama Coast and vicinity. Contours are based on the 5-m-mesh DEM from GSI. Intervals of gray and black contours are 1 m and 5 m, respectively. Curving arrow denotes the channel and flow direction of the Bitsuke River

**Table 1** Historical tsunamis along the Pacific Coast in Hokkaido and Tohoku regions during 1611–2003 CE

| Date [CE] | Tsunami name | Source | Magnitude (Utsu 2004) | Tsunami height (m) | Location of measured site |
|---|---|---|---|---|---|
| 2003 | Tokachi-oki | Off Tohoku | 8.0 | 1.5–2.4[1] | West and south of Shiriyazaki |
| 1994 | Shikotan-oki | Off Shikotan | 8.2 | < 1[2] | Northern part of the Shimokita peninsula |
| 1968 | Tokachi-oki | Off Tohoku | 7.9 | < 2[2] | East coast of the Shimokita peninsula |
| 1960 | Chile | Chile | 9.5 | 1[2] | East coast of the Shimokita peninsula |
| 1952 | Tokachi-oki | Off Tohoku | 8.2 | (2)[2] | Hachinohe |
| 1933 | Showa-Sanriku | Off Tohoku | 8.1 | 1[2] | Sekinehama |
| 1896 | Meiji-Sanriku | Off Tohoku | 8.2 | (3)[2] | Hachinohe |
| 1856 | Ansei | Off Tohoku | 7.7 | 1.5[3] | Between Ohmazaki and Sekinehama |
| 1843 | Tempo | Off Nemuro | 8.0 | (2)[3] | Hakodate |
| 1763 | Horeki | Off Tohoku | 7.7 | (1)[3] | Hachinohe |
| 1677 | Empo | Off Tohoku | 7.9 | 1.7–2.9[3] | Between Ohmazaki and Sekinehama |
| 1611 | Keicho | Off Tohoku | 8.1 | – | |
| 1741 | Oshima-Oshima | Oshima-Oshima volcano | Related to volcanic event | – | |
| 1640 | Komagatake | Komagatake volcano | Related to volcanic event | – | |

1: Tanioka et al. (2004); 2: Watanabe (1998); and 3: Tsuji et al. (2014)

The numbers in parentheses in "Tsunami height" column indicate the values at sites away from Sekinehama

tsunami with the 1611 Keicho tsunami has been debated but is not yet fully understood (e.g., Tetsuka et al. 2020).

From research in the vicinity of the study site, two studies, Minoura et al. (2013) and Tanigawa et al. (2014), identified tsunami deposits along the east coast of the Shimokita Peninsula (Fig. 1b). Minoura et al. (2013) identified one tsunami deposit as having occurred between the late thirteenth and fifteenth centuries. Tanigawa et al. (2014) identified five sandy event deposits interbedded within marsh deposits during the last 6000 years, three of which were attributed to inundation from the coast on the basis of diatom assemblages. The latest one is estimated to have occurred 470–180 cal yr BP. Along the Sanriku Coast, many tsunami-deposit surveys were conducted after the 2011 event. They show the relatively high frequency of paleotsunamis from the north to the central parts of this coast (Fig. 1), where their average recurrence interval is ~ 300–500 years (Ishimura 2017; Ishimura and Yamada. 2021; Ishizawa et al. 2022; Velasco-Reyes et al. 2022). On the Hokkaido side, many drilling surveys were also conducted. In eastern Hokkaido, a short average recurrence interval (close to 400 years) was estimated from long-term tsunami history based on the tsunami deposits (e.g., Sawai et al. 2009), whereas prior tsunami-deposit researchers found a longer average recurrence interval to the west of the Hidaka Coast than eastern Hokkaido (Takashimizu et al. 2007; Takashimizu 2014; Nakanishi et al., 2020, 2022). To the west of the Hidaka Coast (Fig. 1a), only one tsunami deposit was identified since ca. 3 ka and was correlated with the seventeenth-century tsunami (Takashimizu et al. 2007). Additionally, the lateral correlation and sources of the tsunami

deposits formed during the last 500 years in the west of the Hidaka Coast (Fig. 1a) are not well understood (Takashimizu 2014). Recently, Kase et al. (2022) reported tsunami deposits around Hakodate on the opposite side of the Tsugaru Strait from the study area (Fig. 1a). They drilled at four sites and identified tsunami deposits formed since ~ 3000 cal yr BP.

## 3 Methods

We conducted a field survey to log two outcrops (SKN-E and SKN-W) along the Sekinehama Coast and cores drilled along the incised valley, which is a subsidiary of the Bitsuke River (Fig. 1c). An additional coring survey was conducted in the south of the SKN-W outcrop to observe the younger sediments. A handy-Geoslicer (GS) (Takada et al. 2002) was used for the coring survey, by which we obtained a total of 11 GS cores.

For nondestructive analyses, we extracted block samples from outcrops and GS cores with a 50-cm-long, 4-cm-wide, and 3-cm-thick case. These block samples were used for X-ray computed tomography (XCT) and high-resolution micro-X-ray-fluorescence (μXRF) scanning at the Center for Advanced Marine Core Research, Kochi University. The XCT images were taken by using an Aquilion PRIME/Focus Edition scanner (Canon Medical Systems Corporation). For this analysis, a sample was imaged according the X-ray absorption so that high-density materials could be identified by their relatively light color (Falvard and Paris 2017). A vertical slice of the block sample was taken every 0.5 mm, and these vertical slices were then processed using Horos software (a free and open-source code software

under the GNU Lesser General Public license, Version 3 (LGPL-3.0)) to build a 3D image of the block sample. Using the ITRAX μXRF core scanner (Croudace et al. 2006), the block sample was measured at 1-mm intervals. The scanner, which irradiated the block sample surface by applying a molybdenum X-ray source, operated at 60 kV and 50 mA and allowed us to obtain data on 30 elements. We used 12 element intensities (Si, S, K, Ca, Ti, Mn, Fe, Ni, Rb, Sr, Y, and Zr) after considering previous studies (Chagué-Goff et al. 2016; Martin-Puertas et al. 2017; Ishizawa et al. 2019). Because the elemental data were influenced by the sample's condition (Löwemark et al., 2011; Chagué-Goff et al. 2016), we normalized each elemental datum over counts per second for comparison between cores (e.g., Davies et al. 2015; Chagué-Goff et al. 2016; Ishizawa et al. 2019).

We determined major element compositions of volcanic glass shards for correlating known tephra. We sampled sediments from GS cores for tephra analysis, while considering the already-identified B-Tm and To-Cu tephras in the coastal outcrops. For the cores with no visible tephra, we conducted continuous sampling and calculated the content of volcanic glass shards. First, we used an ultrasonic generator to rinse the samples in water and then sieved them with water through a 62-μm nylon mesh. Next, we dried the samples at 50 °C and sieved the dried samples through a 120-μm nylon mesh. Then, using a polarizing microscope, we counted volcanic glass shards in the 62–120-μm fraction. Finally, we determined the major element composition of the volcanic glass shards in that size fraction by energy-dispersive X-ray spectrometry (EDAX Genesis APEX2) and scanning electron microscopy (JEOL JSM-6390) following the method and analysis conditions described by Suzuki et al. (2014). Volcanic glass shards of the AT tephra sampled at Chigaki, Toyama Prefecture (Machida and Arai 2013), were used as a working standard to check data reproducibility and instrument stability.

For grain-size analysis, we collected all event-deposit samples from the outcrops and cores, and present-day sediment samples surrounding the study site (Fig. 1c). As for the present beach sediments, we confirmed that there has been no artificial beach nourishment by the interview to the city office. First, each sample was pretreated with 3% $H_2O_2$ to eliminate organic matter and then rinsed with water using an ultrasonic generator. Then, we sieved the samples with water through a 62-μm nylon mesh and then used a 2-mm sieve. Finally, we measured the weight of sand and gravel fractions to calculate mud, sand, and gravel contents. Grain-size analysis of sand fractions was performed using Morphologi G3 (Malvern Instruments Ltd.) according to Ishizawa et al. (2019), but in our study, we used the 5X magnification setting.

Radiocarbon dating using an accelerator mass spectrometer was performed at the Institute of Accelerator Analysis Ltd., Japan. We obtained 42 radiocarbon dates: 32 for samples from GS cores and 10 for samples from outcrops. Radiocarbon dates were calibrated based on the IntCal20 calibration curve (Reimer et al. 2020) using the OxCal 4.4 program (Bronk Ramsey 2009). We used the sequence model (Bronk Ramsey 2008) for calculating depositional ages of tsunami deposits (Additional file 1).

## 4 Results
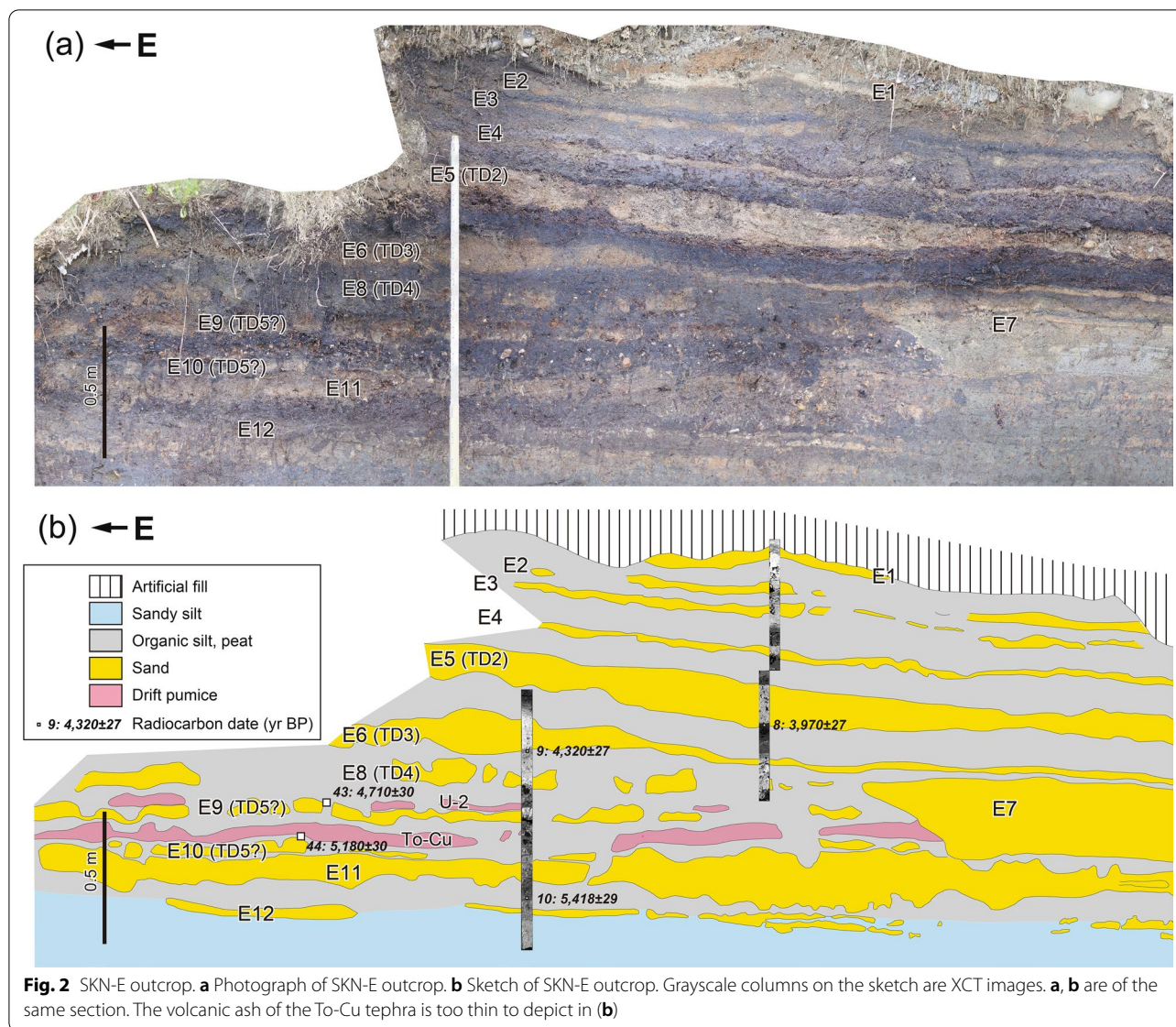### 4.1 Outcrops along the Sekinehama Coast
#### *4.1.1 SKN-E outcrop*
The SKN-E outcrop (Fig. 2) is ~ 300 m east of the mouth of the Bitsuke River (Fig. 1c) and is on a sea cliff that is 2.5 m high and 10 m wide. The sediments exposed in this outcrop apparently belong to two different sedimentary facies. The lower part consists of blue-gray silt (possibly marine sediments), and the upper part includes marsh deposits consisting of organic silt and peat. The uppermost part is artificially modified sediments that contain concrete blocks and fishnets. In this study, we described and sampled sandy event deposits in the marsh sediments.

We recognized 12 sandy event deposits in the SKN-E marsh sediments (SKN-E-E1 to SKN-E-E12, from youngest to oldest) (Fig. 2; Table 2). Except for SKN-E-E7, they show good horizontal continuity. Most consist of well-sorted fine to medium sand. SKN-E-E5, SKN-E-E6, SKN-E-E8, and SKN-E-E9 contain coarser grains such as granules. SKN-E-E5 and SKN-E-E6 have an erosive contact at the base and contain rip-up clasts in the lower part. SKN-E-E8 also contains rip-up clasts. Some of the sandy event deposits show normal grading. The bottom shape of SKN-E-E7 is convex downward, suggesting a channel, and the deposit has parallel laminations.

From the grain-size analysis (Fig. 3), SKN-E-E1 to SKN-E-E4 show grain-size distributions concentrated in the range 1–2 phi. Meanwhile, SKN-E-E5 to SKN-E-E10 show modes of 1–2 phi, but exhibit a wider grain-size distribution. In the event deposits below SKN-E-E11, the mode changes from 1–2 phi to 1.5–2.5 phi with finer grains. This is apparent from the mud content (Fig. 3). The gravel contents also support the above descriptions indicating that SKN-E-E5, SKN-E-E6, and SKN-E-E8 include coarser grains.

Three tephra-related layers in the marsh sediments were already identified (Fig. 2) and described in detail in Ishimura and Hiramine (2020) and Hiramine et al. (in press). To-Cu (5986–5899 cal yr BP) tephra (fine-grained volcanic ash) is interbedded between SKN-E-E9 and SKN-E-E10 (Ishimura and Hiramine 2020), and drift pumice clasts that originated from To-Cu tephra

**Fig. 2** SKN-E outcrop. **a** Photograph of SKN-E outcrop. **b** Sketch of SKN-E outcrop. Grayscale columns on the sketch are XCT images. **a**, **b** are of the same section. The volcanic ash of the To-Cu tephra is too thin to depict in (**b**)

are concentrated above the ash layer (Hiramine et al. in press). Other drift pumice clasts, concentrated between SKN-E-E8 and SKN-E-E9, were correlated with the U-2 tephra (5681–5619 cal yr BP) (Hiramine et al. in press). Furthermore, they suggested that the depositional timings of these pumice concentrated layers are shortly after the eruptions, and thus, their tephra dates can be used as ages of the horizons.

### 4.1.2 SKN-W outcrop

The SKN-W outcrop (Fig. 4) is ~ 150 m east of the mouth of the Bitsuke River and is exposed over a 2 m height and a 1 m width. There are 17 sandy event deposits (SKN-W-E1 to SKN-W-E17, from youngest to oldest) interbedded within organic silt and peat (Fig. 3; Table 2). For

observing the uppermost sandy event deposit, two GS cores (SKN-W-GS1 and SKN-W-GS2) were obtained behind the outcrop. Except for SKN-W-E1 and SKN-W-E8, which are notably thick (> 15 cm), the sandy event deposits are ~ 10 cm thick or less.

Most of the sandy event deposits consist of well-sorted fine-to-medium sand. SKN-W-E1, SKN-W-E2, SKN-W-E11, and SKN-W-E14 include coarse sand. Our detailed observation revealed that the 1–2-cm-thick black layer between SKN-W-E3 and SKN-W-E4 was a sand layer with a little organic material rather than soil. Therefore, SKN-W-E3 and SKN-W-E4 were determined to be a single sandy event deposit (hereinafter SKN-W-E3/4). The bases of SKN-W-E3/4, SKN-W-E11, and SKN-W-E14 are erosive contacts, but the upper and lower boundaries

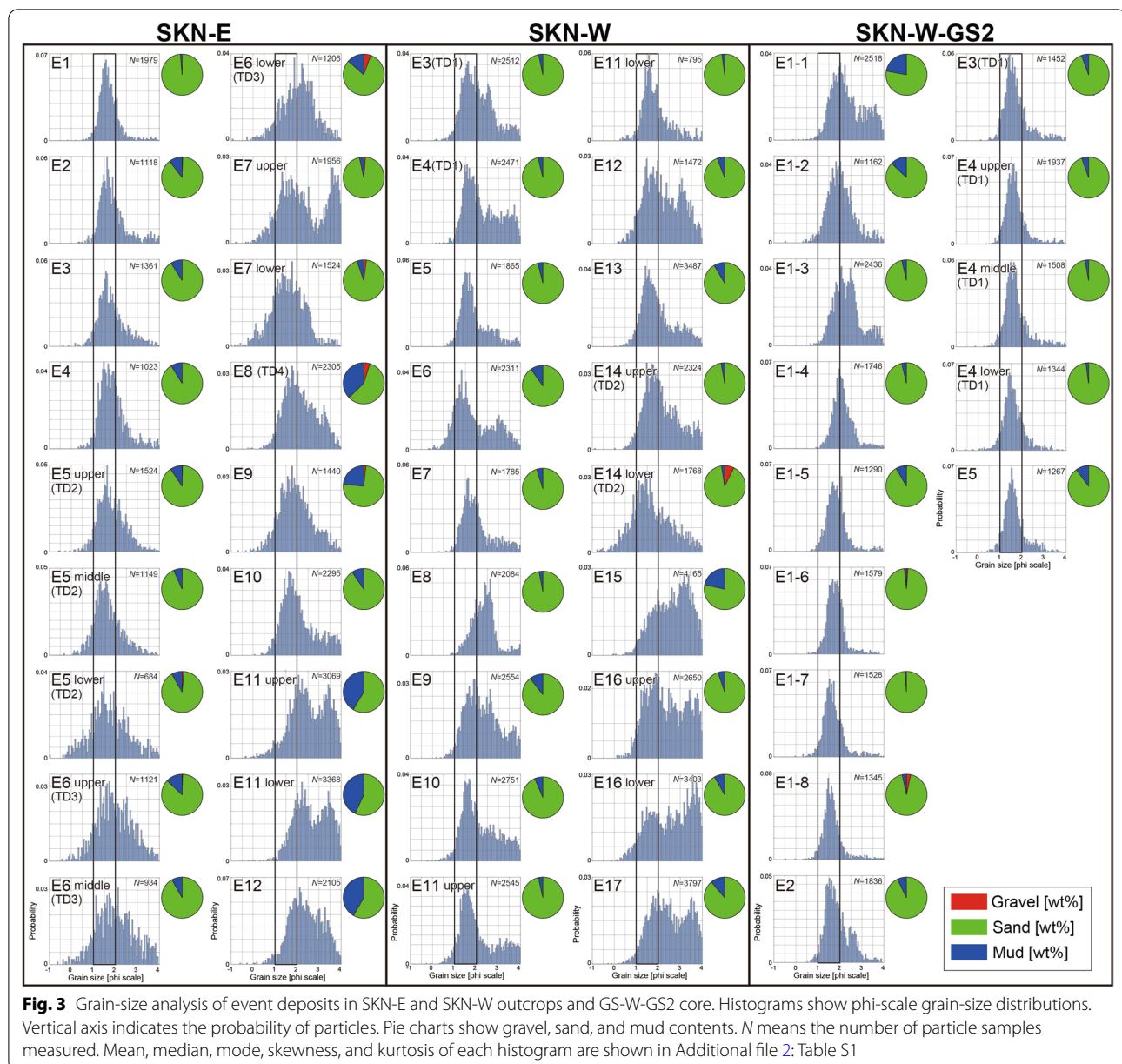**Table 2** Description of sandy event deposits in samples SKN-W, SKN-E, and SKN-GS

| Location | Event no. | Grain size | Thickness (cm) | Sedimentary structure | Interpretation |
|---|---|---|---|---|---|
| SKN-E | E1 | fs, ms | 5 | | |
| | E2 | fs, ms | 3 | | |
| | E3 | fs, ms | 3 | | |
| | E4 | fs, ms | 3 | Normal grading | |
| | E5 | ms-granule | 10–15 | Normal grading, rip-up clasts (< 1 cm), pumice clast (< 1 cm), gravel (2–3 cm) at lower part, erosive contact at base | |
| | E6 | ms-granule | 3–15 | Normal grading, rip-up clasts, gravel (3 cm), erosive contact at base | |
| | E7 | ms, cs | 25–30 | Channel fill, erosion up to E10, parallel laminae | |
| | E8 | ms-vcs | 5–10 | Patchy distribution, normal grading, rip-up clasts | |
| | U-2 (drift pumice) | | | | U-2 (5681–5619 cal yr BP) |
| | E9 | ms-granule | 3–5 | Poor sorting | |
| | To-Cu (drift pumice) | | | | |
| | To-Cu (fallout ash) | | | | To-Cu (5986–5899 cal yr BP) |
| | E10 | ms | 3 | Patchy distribution | |
| | E11 | silt, ms-cs | 10–20 | Matrix rich, a little grading, bioturbation | |
| | E12 | fs, silt | | Matrix rich, patchy distribution | |
| SKN-W | E1 | ms, cs | > 16 | Parallel laminae in the lower part | |
| | E2 | ms, cs | 4 | | |
| | E3 | ms | 6–9 | | |
| | E4 | Ms | 12 | Erosive contact at base | |
| | E5 | ms | 5–10 | | |
| | B-Tm | fs | 2 | Normal grading | B-Tm (946 CE) |
| | E6 | fs | 5 | | |
| | E7 | fs, ms | 5–8 | | |
| | E8 | fs | 6–20 | Parallel laminae | |
| | E9 | fs, ms | 2–4 | | |
| | E10 | fs, ms | 4–8 | Erosive contact at base | |
| | E11 | ms, cs | 6–7 | Normal grading, erosive contact at base | |
| | E12 | ms | 1–5 | | |
| | E13 | ms | 3 | | |
| | E14 | ms, cs | 5–9 | Normal grading, erosive contact at base | |
| | E15 | fs | 1–2 | Not continuous | |
| | E16 | ms | 7–12 | Normal grading | |
| | E17 | ms | 4–10 | | |
| SKN-GS | GS9-E1 | ms | 10 | Composed of 2–3 units, erosive contact at base | |
| | Volcanic ash | fs | 3 | | B-Tm (946 CE) |
| | GS9-E2 | fs, ms | 2–3 | Erosive contact at base | |
| | GS9-E3 | ms | 6 | Erosive contact at base | |
| | GS9-E4 | ms | 4 | Unclear | |
| | GS8-E1 | ms | 13 | Composed of 2–3 units, erosive contact at base | |
| | Volcanic ash | fs | 3 | | B-Tm (946 CE) |
| | Volcanic ash | fs | 2 | Laminae | B-Tm (946 CE) |
| | GS8-E2 | ms | 2 | Erosive contact at base | |
| | GS8-E3 | ms, cs | 5 | Laminae, erosive contact at base | |
| | GS8-E4 | silt-granule | 36 | Erosive contact at base | |
| | GS8-E5 | fs, ms | 3 | Unclear laminae, erosive contact at base | |
| | GS8-E6 | fs, ms | > 3 | Parallel laminae | |
| | GS1-E1 | fs, ms | 15 | Composed of 2–3 units, erosive contact at base | |

**Table 2** (continued)

| Location | Event no. | Grain size | Thickness (cm) | Sedimentary structure | Interpretation |
|---|---|---|---|---|---|
| | Volcanic ash | vfs | 4 | | B-Tm (946 CE) |
| | GS1-E2 | ms | 3 | Unclear laminae, erosive contact at base | |
| | GS1-E3 | ms | 9 | Cross laminae, laminae tilting to inland, erosive contact at base | |
| | GS1-E4 | ms-granule | 52 | Parallel laminae, cross laminae, laminae tilting to seaward, fining upward in the upper part, coarsening upward in the lower part, erosive contact at base | |
| | GS1-E5 | fs | 3 | | |
| | GS1-E6 | fs | 1 | | |
| | GS7-E1 | ms | 13 | Composed of 2–3 units, erosive contact at base | |
| | Volcanic ash | fs | < 1 | Patchy distribution | B-Tm (946 CE) |
| | GS7-E2 | fs | 1 | Unclear, identified in XCT image | |
| | GS7-E3 | ms-granule | 45 | Parallel laminae, cross laminae, laminae tilting to seaward, fining upward in the upper part | |
| | GS7-E4 | ms, cs | > 5 | | |
| | GS6-E1 | ms | 12 | Composed of 2–3 units, erosive contact at base | |
| | Volcanic ash | fs | 2–3 | | B-Tm (946 CE) |
| | GS6-E2 | ms, cs | 1 | Erosive contact at base | |
| | GS6-E3 | ms, cs | 8 | Cross laminae, laminae tilting to inland, normal grading, erosive contact at base | |
| | GS6-E4 | ms | 1 | Erosive contact at base | |
| | GS6-E5 | vcs | 12 | Erosive contact at base | |
| | GS6-E6 | ms, cs | 5 | Cross laminae, laminae tilting to inland, erosive contact at base | |
| | GS6-E7 | vcs, granule | 3 | Contain rounded gravel, erosive contact at base | |
| | GS5-E1 | ms, fs | 1 | | |
| | GS5-E2 | ms, fs | 7 | Erosive contact at base | |
| | GS5-E3 | csms | 15 | Composed of 2–3 units | |
| | GS5-E4 | ms-granule | 5 | Contain rounded gravel, normal grading, erosive contact at base | |
| | GS5-E5 | ms-vcs | 6 | Inversegrading, unclear laminae, erosive contact at base | |
| | GS5-E6 | ms | 4 | Erosive contact at base | |
| | GS4-E1 | ms, fs | 1 | Patchy distribution | |
| | GS4-E2 | ms, fs | 3 | Composed of 2 units | |
| | GS4-E3 | ms, fs | 1 | Patchy distribution | |
| | GS4-E4 | fs | 5 | Unclear, identified in XCT image | |
| | GS4-E5 | ms, cs | 18 | Composed of 2–3units | |
| | GS4-E6 | fs-granule | 53 | Composed of multiple units, fining upward in the upper part, coarsening upward in the lower part, erosive contact at base | |
| | GS3-E1 | ms | 6 | Patchy distribution | |
| | Volcanic ash | fs | 10 | Unclear, identified in XCT image | B-Tm (946 CE) |
| | GS3-E2 | fs | 2 | Unclear, identified in XCT image | |
| | GS3-E3 | ms | 1 | | |
| | GS2-E1 | fs, ms | 10 | Unclear, identified in XCT image | |
| | Volcanic ash | fs | 5 | | B-Tm (946 CE) |
| | GS2-E2 | fs, ms | 1 | Erosive contact at base | |
| | GS2-E3 | fs, ms | 10 | Erosive contact at base | |
| | GS2-E4 | fs, ms | 10 | Erosive contact at base | |
| | GS2-E5 | fs, ms | 3 | Unclear parallel laminae, erosive contact at base | |

Tephra ages are based on Oppenheimer et al. (2017) and Mclean et al. (2018)

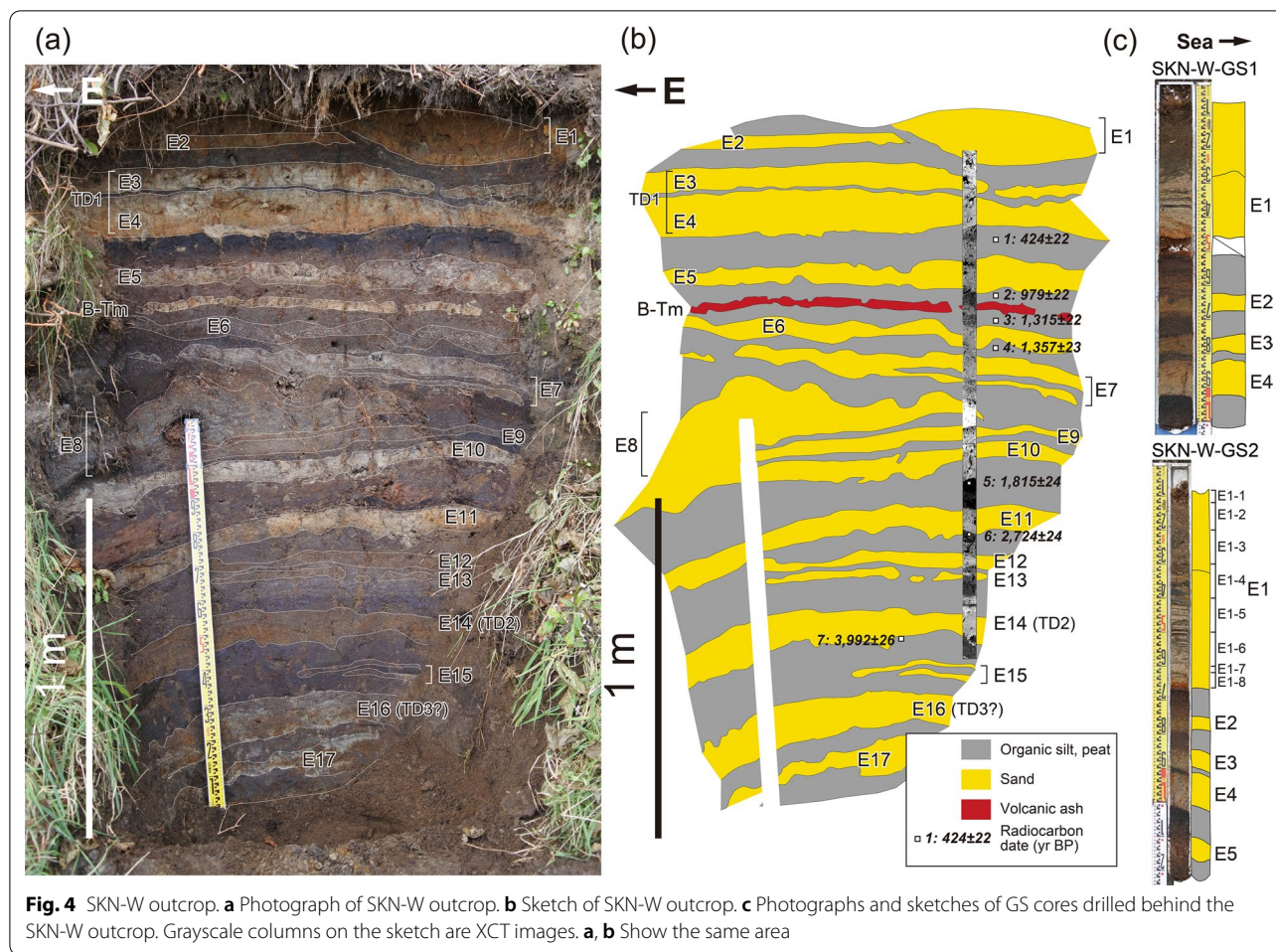*vfs* very fine sand, *fs* fine sand, *ms* medium sand, *cs* coarse sand, *vcs* very coarse sand

**Fig. 3** Grain-size analysis of event deposits in SKN-E and SKN-W outcrops and GS-W-GS2 core. Histograms show phi-scale grain-size distributions. Vertical axis indicates the probability of particles. Pie charts show gravel, sand, and mud contents. *N* means the number of particle samples measured. Mean, median, mode, skewness, and kurtosis of each histogram are shown in Additional file 2: Table S1

of other event deposits are unclear. We recognized normal grading in SKN-W-E11, SKN-W-E14, and SKN-W-E16, whereas SKN-W-E1 and SKN-W-E8 characteristically have multiple parallel laminae. The GS cores behind the outcrop also show alternating layers of light and heavy minerals in the lower part of SKN-W-E1, while the upper part is massive owing to bioturbation (Fig. 4c).

In the grain-size analysis (Fig. 3), almost all event deposits show a mode at 1–2.5 phi, but their distribution ranges are variable. Below SKN-W-E14, event deposits contained more fine sand fractions compared

to those above it. The event deposits in SKN-W-GS2 show a very sharp mode from SKN-W-E1 to SKN-W-E5. The upper part of SKN-W-E1 has more fine-grained material compared to its lower part, possibly influenced by bioturbation and aeolian deposits.

We recognized the volcanic ash layer between SKN-W-E5 and SKN-W-E6 that was already correlated with B-Tm tephra (946 CE; Oppenheimer et al., 2017) by Kobayashi (2019), who also detected volcanic glass shards of To-a tephra (915 CE; Machida and Arai 2013) from the lower part of B-Tm tephra, suggesting that the

**Fig. 4** SKN-W outcrop. **a** Photograph of SKN-W outcrop. **b** Sketch of SKN-W outcrop. **c** Photographs and sketches of GS cores drilled behind the SKN-W outcrop. Grayscale columns on the sketch are XCT images. **a**, **b** Show the same area

age of sediments above and below this tephra is post-946 CE and pre-915 CE, respectively.

### 4.2 Cores drilled in the incised valley

Nine GS cores (SKN-GS1 to SKN-GS9) were obtained 200–400 m inland from the shore (Figs. 1c, 5). Coring depths were 1.3–2.8 m. We cut 50-cm-length block samples from each core for nondestructive analysis. Except for SKN-GS2, the sediments mainly consisted of organic-rich sediments (marsh deposits) with interbedded sandy event deposits. Only SKN-GS2 contains a massive grayish-white clay at deeper than ~2.6 m depth.

We recognized sandy event deposits consisting of a single unit or multiple units. Many of the single-unit deposits were well sorted but lacked any sedimentary structures. SKN-GS1-E3, SKN-GS6-E3, and SKN-GS6-E-6 characteristically have laminae that tilt inland. We interpreted that these laminae may be cross lamination by considering the relationship between the bedding plane and laminae and by taking into account the some deformations (e.g., dragging) due to GS coring,

although the observation window of GS cores is narrow compared to outcrops. Therefore, they indicate that the paleocurrent direction was from seaside to inland (Fig. 6). The multiunit deposits were further divided into thin (< 10–20 cm) and thick (> 35 cm) deposits. Among the multiunit event deposits, thin layers were indistinct to the naked eye but could be identified clearly on XCT images. The uppermost event deposit (E1 in each core) consists of a lower visible sand layer and one or two unclear sand layers that can be recognized in XCT images taken at the seaward sites but that show as a single sand layer at the inland sites (Figs. 5, 6). Four multiunit event deposits (SKN-GS1-E4, SKN-GS4-E6, SKN-GS7-E3, and SKN-GS8-E4) with notable thicknesses (> 35 cm) exhibit alternations of coarse-grained and fine-grained layers. The sedimentary structures of SKN-GS1-E4 and SKN-GS7-E3 show clear cross laminations, indicating a seaward paleocurrent, while those of SKN-GS8-E4 and SKN-GS4-E6 are indistinct, possibly owing to bioturbation.
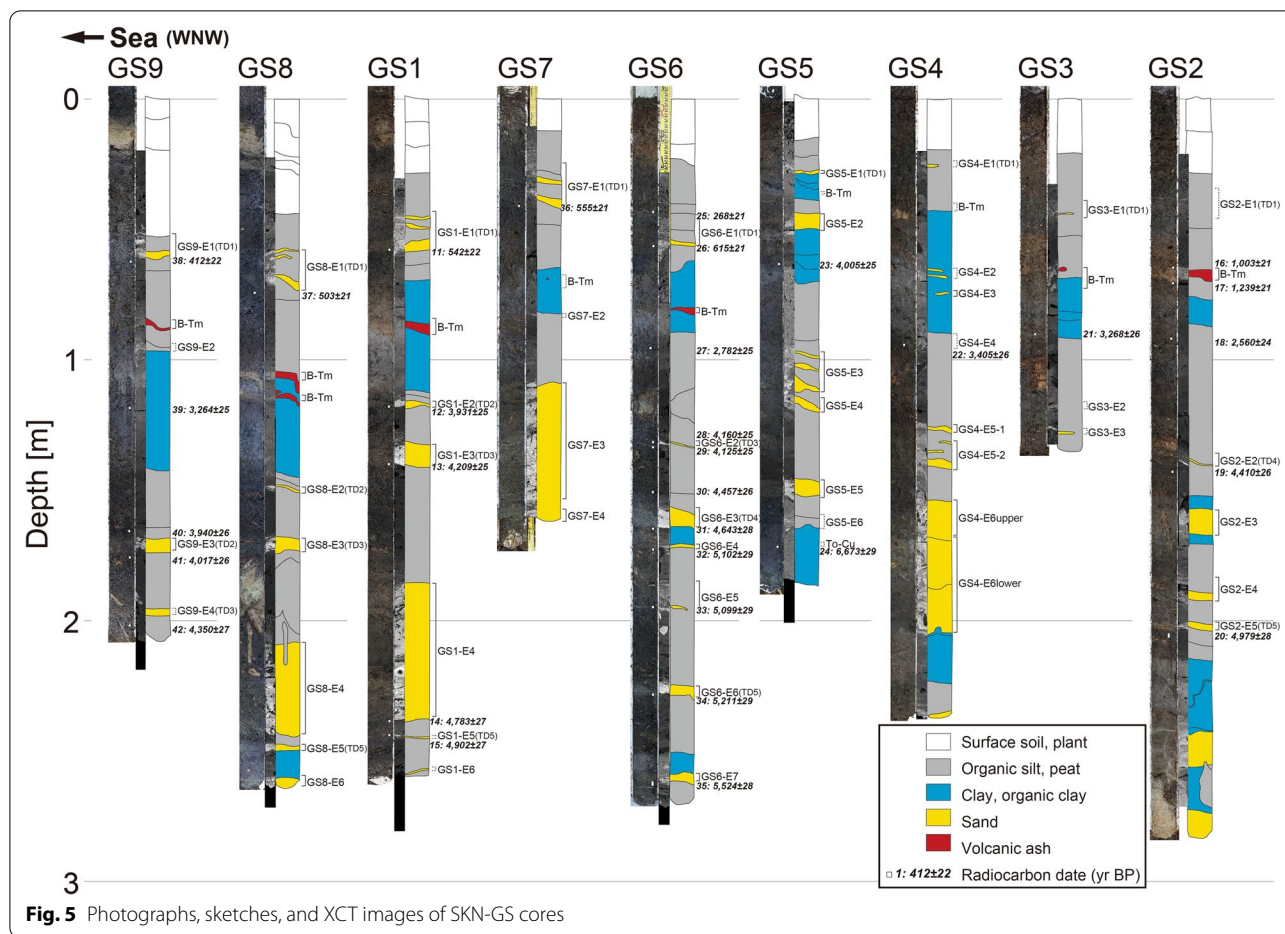
**Fig. 5** Photographs, sketches, and XCT images of SKN-GS cores

From the tephra analysis, we identified visible tephra layers and volcanic glass concentrated horizons (Table 3). Visible tephra layers were identified below E1 deposits in all SKN-GS cores except for SKN-GS4 and SKN-GS5, for which continuous sampling revealed volcanic glass concentrated horizons (Fig. 5, Table 3). The volcanic glass shards in the visible tephra layers and volcanic glass concentrated horizons below E1 deposits in all cores show mainly platy-type morphology. However, the horizon at 170–172 cm depth in SKN-GS5 showed the highest volcanic glass content within 163–186 cm depth (Table 3). The volcanic glass shards at that horizon have a pumiceous (highly vesiculated) morphology.
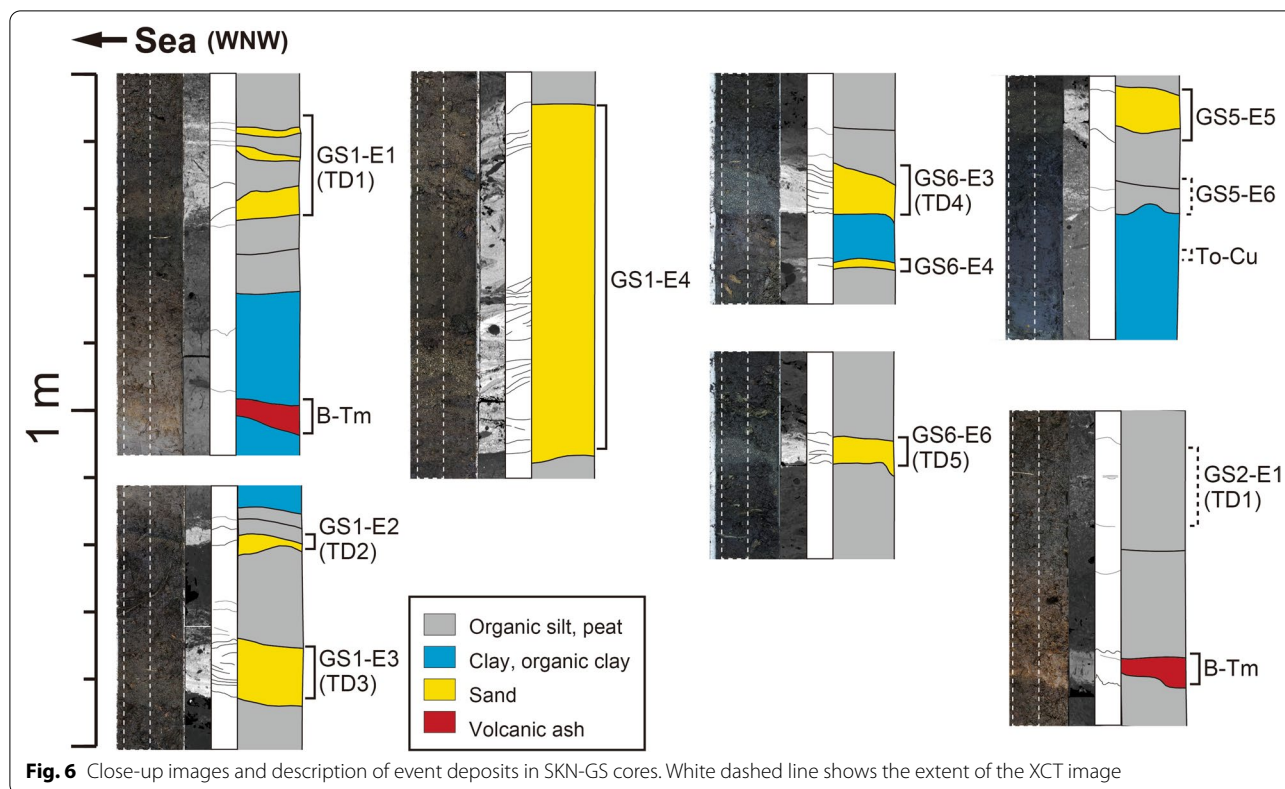
The results of the grain-size analyses of the SKN-GS samples (Fig. 7) show more variety than those of the coastal outcrops SKN-E and SKN-W. Three types were observed: sandy event deposits with a 1–2-phi mode and a narrow grain-size distribution, those with a 3–4-phi mode and a wide grain-size distribution, and those with a bimodal mode (1–2 phi and 3–4 phi). Some SKN-GS samples contained a large amount of mud, but this may be owing to the bioturbation and indistinct sand layers.

The uppermost E1 deposit in all cores with the same stratigraphic position (above the visible tephra or volcanic glass concentrated horizon) has the same grain-size distributions.

According to the ITRAX analysis results (Fig. 8 and Additional file 2: Fig. S1) for the 12 elements that we investigated, the values of Si, K, Ca, Ti, Mn, Fe, and Sr are higher in the sand layers. In the visible tephra layers and volcanic glass concentrated horizons below E1 deposits, K and trace elements (Rb, Y, and Zr) characteristically increase. Data for Ni are somewhat noisy but are macroscopically stable. S is slightly elevated in a few event deposits (SKN-GS1-E3, SKN-GS1-E6, and SKN-GS6-E6 in Fig. 8).

### 4.3 Grain-size analysis of present-day sediments

We did grain-size analysis of present-day sediments (Figs. 1c, 9) surrounding the study site to compare with event deposits in the outcrops and SKN-GS cores. We included foreshore and backshore beach sediments, aeolian sediments, Pleistocene marine-terrace deposits, and fluvial sediments in the incised valley where we

**Fig. 6** Close-up images and description of event deposits in SKN-GS cores. White dashed line shows the extent of the XCT image

obtained SKN-GS cores. We first observed the grain compositions and particle shapes of present-day sediments, which were composed mainly of quartz, pyroxenes, and rounded rock fragments with weathering rind. The volcanic rocks and tephras from the volcanoes located at the west of the study site contain quartz and pyroxenes (Tsushima and Takizawa 1977); thus, sources of the sediments are primarily the ejecta of volcanoes. Furthermore, our findings suggest no substantial differences in the type and shape of the particles that comprise any deposits; therefore, the grain-size distribution is considered important for determining the source of the sediments.

The foreshore sediments show a mode in the range 1.5–2.5 phi and are characterized by a narrow grain-size distribution. The backshore sediments contain finer-grained particles (3–4 phi), which may reflect a contribution of aeolian sand. Aeolian sediments on the Pleistocene marine terrace have multiple modes: 2-phi, 2.5-phi, and 3–4-phi particles. These finer-grained particles are thought to be the result of wind-driven transport. The mode of the Pleistocene marine-terrace deposits is similar to that of present-day beach sediments but has a wider grain-size distribution and contains coarser particles. Fluvial sediments from the creek in the incised valley show a similar size distribution to that of the

Pleistocene marine-terrace deposits, which is consistent with the creek's having incised the terrace.

## 5 Discussion
### 5.1 Tephra correlation
Using the major element compositions of volcanic glass shards (Table 4; Additional file 2: Fig. S2), the visible tephra at the 88–89 cm depth in SKN-GS1 was correlated with B-Tm tephra in SKN-W, and the volcanic glass concentration horizon at the 170–172 cm depth in SKN-GS5 included volcanic glass shards of To-Cu tephra. The former result means that the visible tephra layers and volcanic glass concentrated horizons below E1 deposits in all GS cores are B-Tm tephra based on the stratigraphic position and similarity of the morphology of volcanic glass shards. Additionally, Nara et al. (2021) reported that the B-Tm tephra characteristically included $K_2O$ and trace elements, which is consistent with our tephra correlations and ITRAX results (Fig. 8 and Additional file 2: Fig. S1). The latter means that the horizon at the 170–172 cm depth in SKN-GS5 is interpreted to be deposited at least after the To-Cu tephra (5986–5899 cal yr BP) as there is a possibility of its secondary deposition. Although two visibly separate volcanic ash layers were identified at the 108–111 cm and 115–117 cm depths in SKN-GS8, their volcanic glass morphology and grain

Ishimura *et al. Progress in Earth and Planetary Science* (2022) 9:69

Page 13 of 27

**Table 3** Tephra-analysis samples

| GS no. | Depth (cm) | Volcanic glass content (%) | Visible (V) or invisible (I) | Correlative tephra |
|--------|-----------|---------------------------|------------------------------|--------------------|
| GS9 | 86.5–89 | 86.0 | V | B-Tm |
| GS8 | 108–111 | 88.8 | V | B-Tm |
| GS8 | 115–117 | 90.0 | V | B-Tm |
| GS1 | 87–89 | 90.0 | V | B-Tm |
| GS7 | 67–68 | 88.2 | V | B-Tm |
| GS7 | 70–72 | 85.0 | I | B-Tm |
| GS6 | 83–85 | 76.4 | V | B-Tm |
| GS5 | 8–10 | 4.4 | – | |
| GS5 | 13–15 | 4.9 | – | |
| GS5 | 18–19 | 10.5 | – | |
| GS5 | 36–37 | 41.9 | I | B-Tm |
| GS5 | 163–165 | 17.1 | – | |
| GS5 | 165–167 | 24.5 | – | |
| GS5 | 167–170 | 22.1 | – | |
| GS5 | 170–172 | 27.3 | I | To-Cu |
| GS5 | 172–174 | 23.1 | – | |
| GS5 | 174–177 | 13.3 | – | |
| GS5 | 177–180 | 11.1 | – | |
| GS5 | 184–186 | 7.7 | – | |
| GS4 | 40–43 | 54.5 | I | B-Tm |
| GS4 | 50–53 | 28.2 | – | |
| GS4 | 58–61 | 16.5 | – | |
| GS3 | 72–73 | 82.4 | V | B-Tm |
| GS2 | 68–71 | 90.0 | V | B-Tm |

compositions are similar, and therefore, we interpreted that both are B-Tm tephra and the lower tephra might have migrated downward by bioturbation.

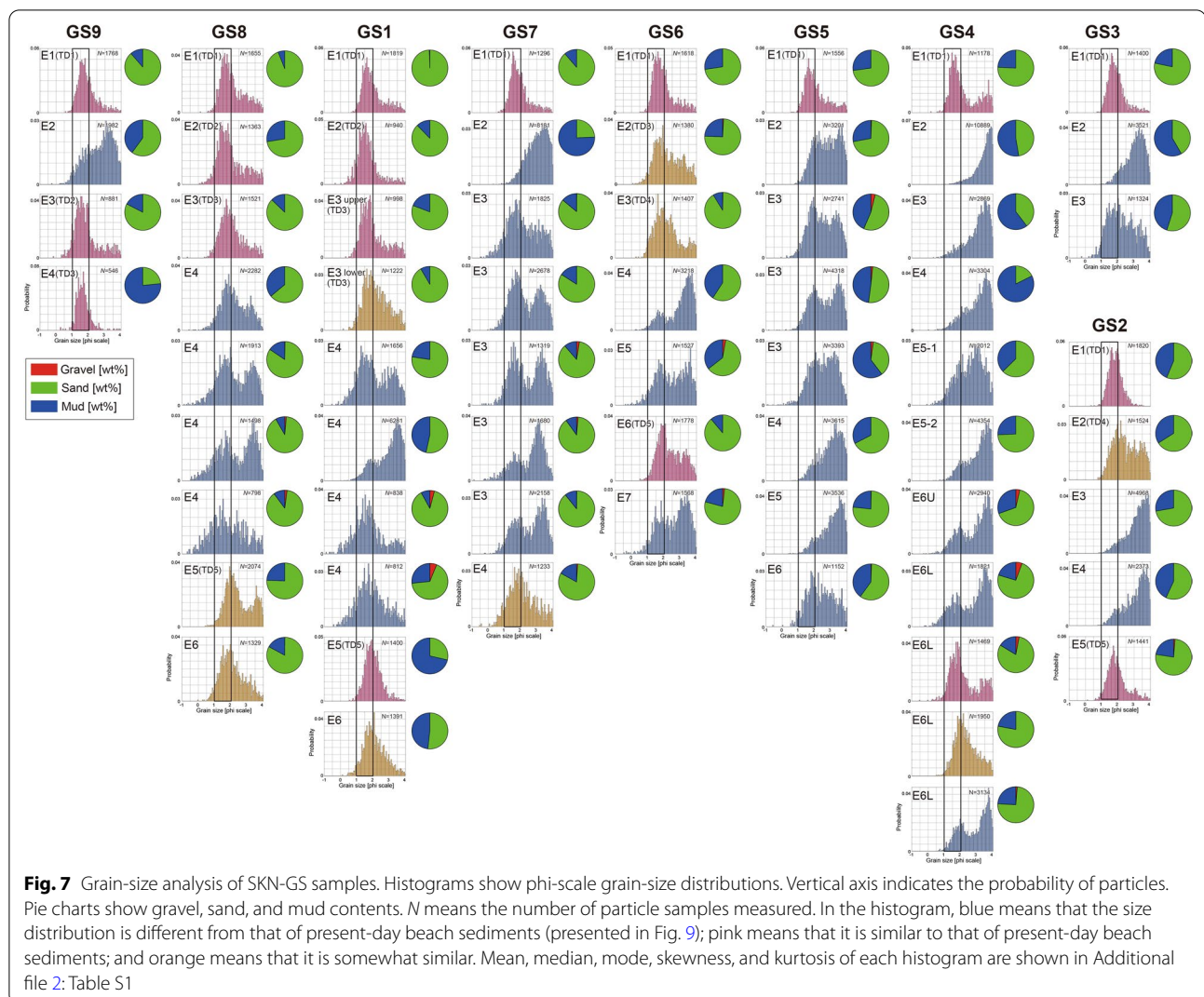### 5.2 Cross-checking radiocarbon dates of organic bulk sediments

Because appropriate measurable organic materials (e.g., seed and leaf) were not available, we used organic bulk sediments for radiocarbon dating (Table 5). When dating organic bulk sediments, if the origin of the organic material is uncertain, it must be cross-checked with known ages. Therefore, in this study, the organic bulk sediments were dated in the To-Cu horizon of SKN-GS5 and horizons above and below the B-Tm tephra in SKN-GS2. As a result, the dates of the upper and lower parts of the B-Tm tephra in SKN-GS2 were $1003 \pm 21$ yr BP (960–800 cal yr BP) and $1239 \pm 21$ yr BP (1270–1070 cal yr BP), respectively, which are consistent with the tephra age. However, the To-Cu volcanic glass concentrated horizon of SKN-GS5 has an age of $6673 \pm 29$ yr BP (7610–7470 cal yr BP), which is older than the To-Cu tephra (5986–5899 cal yr BP). Because we expected that the horizon contained secondary deposits of To-Cu tephra, we assumed that

a younger age than the tephra would not be a problem, but the obtained age is older than the tephra age. Therefore, we considered the possibility that old carbon was included in the horizon. Although by visual inspection we thought the sedimentary facies consisted of clay-rich sediments (Fig. 6), the sedimentary structure from the XCT indicated that it was a poorly sorted clay with sand, indicating that the sediments were transported by fluvial processes and contained old carbon. The horizons above and below B-Tm tephra are organic-rich sediments containing few sand grains (Fig. 6). Because organic-rich sediments deposited in a stable environment provide a more accurate age, we chose the horizon with little old organic carbon for radiocarbon dating of organic bulk sediments. We determined that horizons with less flow-in by fluvial processes (i.e., with fewer clastic particles) were those with less old organic carbon and used XCT images to select such horizons. Therefore, some radiocarbon dates were obtained at some distance from the event deposits (Fig. 5).

### 5.3 Paleogeography of Sekinehama

Before the identification of the tsunami deposits, we looked at the topographic change around the study site since ~ 6 ka. Using an aerial photograph taken in 1952 and a corresponding geomorphic classification (Fig. 10a, b), we reconstructed the paleogeography of Sekinehama. The 1952 aerial photograph shows that dunes used to be distributed along the coast where currently the front of the coastal outcrops are located, while the other aerial photographs show that the topography in 2001 was almost the same as today. This suggests that the outcrops that we studied appeared at the surface owing to coastal erosion in the last 50 years. Thus, until more than 50 years ago, these outcrops had been in a lowland behind the coastal dune and unexposed.

Hiramine et al. (in press) found two layers composed of abundant drift pumice in SKN-E and concluded that SKN-E was under a lagoon-like wetland environment connected to the sea via a small channel at ~ 6 ka (Fig. 10c). The presence of drift pumice and underlying marine sediments at SKN-E roughly indicates a paleo-sea level at 2 m above the present sea level (Hiramine et al. in press). Okuno et al. (2014) showed that theoretical relative sea level is 0–2 m in 6 ka at Ominato (15 km southwest from the study site), indicating that study cite is stable or slightly uplifted during the last 6 ka. This tendency is consistent with the long-term uplift rate of 0.1–0.2 mm/yr based on the MIS 5 marine-terrace surfaces (Koike and Machida 2001). Even if this uplift is taken into account, the sediments in the GS cores are considered to be higher in elevation than the sea level at that time.

**Fig. 7** Grain-size analysis of SKN-GS samples. Histograms show phi-scale grain-size distributions. Vertical axis indicates the probability of particles. Pie charts show gravel, sand, and mud contents. *N* means the number of particle samples measured. In the histogram, blue means that the size distribution is different from that of present-day beach sediments (presented in Fig. 9); pink means that it is similar to that of present-day beach sediments; and orange means that it is somewhat similar. Mean, median, mode, skewness, and kurtosis of each histogram are shown in Additional file 2: Table S1

From the above-estimated paleogeography, the coastline at ~6 ka was estimated to be more seaward than at present, indicating that the present coastline position is the nearest position to the GS core sites during the last 6 kyrs. Additionally, the layers of the drift pumice indicate the paleoshoreline position of ~6 ka in the inland lagoonal environment (SKN-E), meaning that there is a distance of at least 200 m from the paleoshoreline of the lagoon behind the spit or dune (Figs. 10c, 11) to the GS core site and that there is a greater distance from the coastline facing the sea (Tsugaru Strait). Although we could not collect additional data on the paleogeography after 6 ka, we interpreted that the study area has tended to be land from 6 ka; therefore, the marine influence has decreased. Additionally, the estimated tidal inlet was limited, and the GS core site was far from it (Fig. 10c). Therefore, a storm is not likely to reach the GS core site after 6 ka.

## 5.4 Interpretation of event deposits in GS cores

We compared source sediments surrounding the study site with event deposits in the GS cores. From the grain-size analysis of source sediments, only the beach sediments show a mode of 1.5–2.5 phi with a narrow grain-size distribution (Fig. 9). This indicates that the sandy event deposits with a grain-size distribution similar to that of present-day beach sediments might have been transported from the beach (pink histograms in Fig. 7). However, coarse-grained sandy event deposits (including -1 to 1 phi particles) with a wider grain-size distribution likely originated from the Pleistocene marine-terrace deposits and are similar to creek sediments. Therefore, they are estimated to be deposited by fluvial processes. Conversely, fine-grained particles (3–4 phi) could be derived from fine sediments above and below event deposits due to bioturbation. If they are mixed by bioturbation to event deposits, especially thin event deposits,
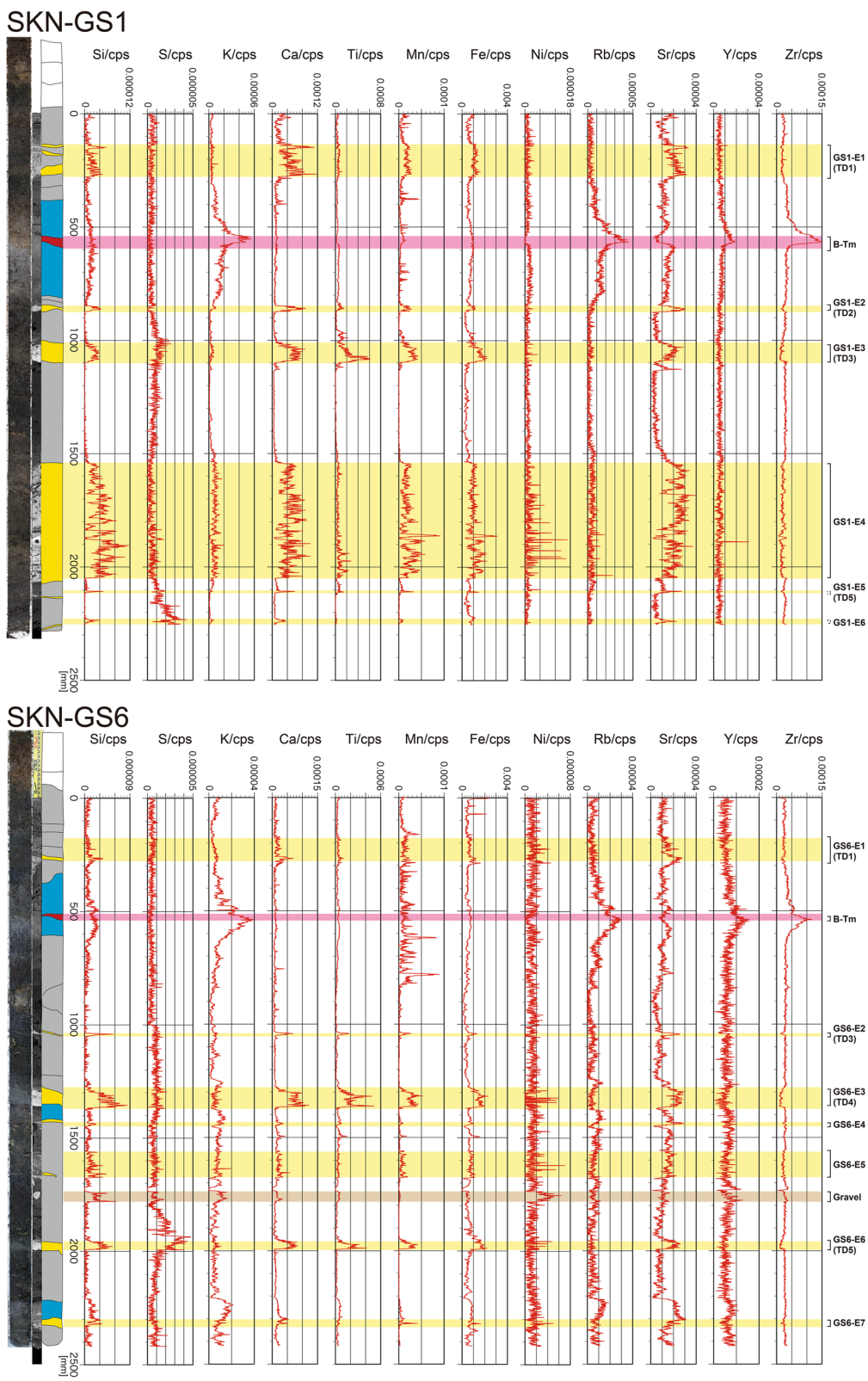
**Fig. 8** Results of the ITRAX micro-X-ray-fluorescence core scanning of SKN-GS1 and SKN-GS6. Each elemental datum was normalized by counts per second (cps)
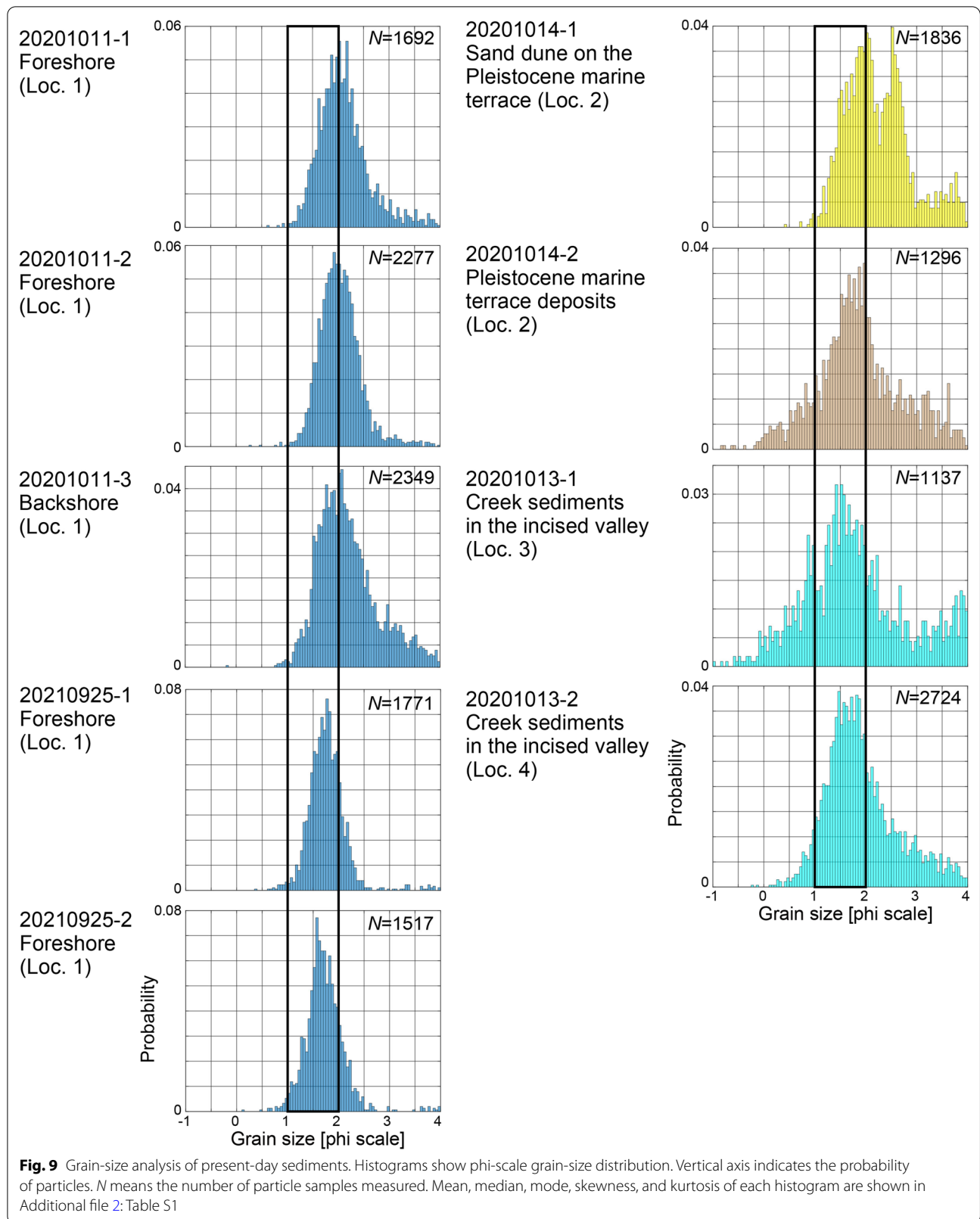
**Fig. 9** Grain-size analysis of present-day sediments. Histograms show phi-scale grain-size distribution. Vertical axis indicates the probability of particles. *N* means the number of particle samples measured. Mean, median, mode, skewness, and kurtosis of each histogram are shown in Additional file 2: Table S1

**Table 4** Major element compositions of volcanic glass shard samples and the AT tephra working standard

| Sample | SiO$_2$ | TiO$_2$ | Al$_2$O$_3$ | FeO" | MnO | MgO | CaO | K$_2$O | Na$_2$O | n | Total"" | Remark |
|---|---|---|---|---|---|---|---|---|---|---|---|---|
| B-Tm ash in SKN-W (1) | 75.0 | 0.2 | 10.9 | 4.0 | 0.1 | ~ ~01 | 0.3 | 4.3 | 5.1 | 8 | 96.5 | |
| | 0.6 | 0.1 | 0.3 | 0.1 | 0.1 | 0.0 | 0.1 | 0.2 | 0.1 | | 0.6 | |
| B-Tm ash in SKN-W (2) | 67.6 | 0.4 | 15.1 | 4.5 | 0.2 | 0.2 | 1.1 | 5.1 | 5.6 | 12 | 97.5 | |
| | 1.2 | 0.1 | 0.5 | 0.2 | 0.1 | 0.1 | 0.3 | 0.2 | 0.2 | | 0.5 | |
| 88–89 cm in depth of SKN-GS1 (1) | 74.8 | 0.2 | 11.0 | 4.0 | 0.1 | 0.1 | 0.3 | 4.5 | 5.0 | 6 | 96.0 | |
| B-Tm | 0.7 | 0.1 | 0.3 | 0.1 | 0.1 | 0.0 | 0.2 | 0.3 | 0.2 | | 0.9 | |
| 88–89 cm in depth of SKN-GS1 (2) | 67.8 | 0.4 | 15.0 | 4.6 | 0.2 | 0.2 | 1.1 | 5.1 | 5.6 | 14 | 97.4 | |
| B-Tm | 1.1 | 0.1 | 0.5 | 0.2 | 0.1 | 0.1 | 0.2 | 0.2 | 0.1 | | 0.7 | |
| 170–172 cm in depth of SKN-GS5 | 74.7 | 0.5 | 13.6 | 2.5 | 0.2 | 0.7 | 2.6 | 1.2 | 4.0 | 19 | 96.6 | |
| To-Cu | 0.3 | 0.1 | 0.3 | 0.3 | 0.1 | 0.1 | 0.1 | 0.1 | 0.2 | | 0.7 | |
| 170–172 cm in depth of SKN-GS5 | 77.9 | 0.2 | 12.5 | 1.4 | 0.1 | 0.3 | 1.7 | 2.5 | 3.4 | 11 | 97.4 | |
| Other tephra | 0.4 | 0.1 | 0.4 | 0.3 | 0.1 | 0.0 | 0.3 | 0.4 | 0.1 | | 1.6 | |
| AT | 78.0 | 0.1 | 12.5 | 1.3 | 0.1 | 0.2 | 1.1 | 3.2 | 3.5 | 24 | 93.9 | |
| Working standard | 0.4 | 0.1 | 0.1 | 0.1 | 0.1 | 0.0 | 0.1 | 0.1 | 0.1 | | 1.4 | |
| To-Cu ash in SKN-E | 74.5 | 0.5 | 13.5 | 2.5 | 0.2 | 0.7 | 2.7 | 1.2 | 4.0 | 16 | 98.7 | Ishimura and Hiramine (2020) |
| | 0.3 | 0.1 | 0.3 | 0.1 | 0.1 | 0.1 | 0.1 | 0.1 | 0.1 | | 0.6 | |

The number on the upper line is the mean value and that on the lower line is the standard deviation. Measured values were recalculated to 100% on a water-free basis. FeO*, total iron oxide as FeO. Total**, raw data before recalculation

grain-size distribution becomes a little wider than the present beach sediments, such as SKN-GS1-E6, or shows bimodal distribution, such as SKN-GS8-E5. If the contribution of fine-grained particles is minor, this possibility should be considered in the determination of source sediments. Therefore, for thin event deposits, it is possible that the fine-grained component, if present, originally had a grain-size distribution similar to that of the present beach sand (orange histograms in Fig. 7). These two event-deposit types (pink and orange histograms in Fig. 7) are candidates for tsunami deposits, as discussed below.

Some event deposits whose grain-size distributions are similar to present-day beach sediments show cross lamination tilting inland (SKN-GS1-E3, SKN-GS6-E3, and SKN-GS6-E6), indicating a paleocurrent directed inland. Furthermore, SKN-GS1-E3, SKN-GS6-E3, and SKN-GS6-E6 show sharp basal contacts, indicating erosional surfaces. These features indicate that they were deposited by the strong flow from the coast. Considering the distance from the coast and estimated paleogeography since ~ 6 ka (Fig. 10c) as discussed in Sect. 5.3, they were deposited by tsunamis rather than storm surges. The E1 deposits above the B-Tm tephra in each core also show almost the same grain-size distribution as the present-day beach sediments, thin inland, and have multiple sand layers. These characteristics also suggest that they are a tsunami deposit and were formed by multiple waves. Because other event deposits do not show any

relevant features other than grain-size distributions, we interpret them based on their distribution in the incised valley. We discuss their correlations between GS cores using radiocarbon dating later in this section.

SKN-GS1-E4, SKN-GS4-E6, SKN-GS7-E3, and SKN-GS8-E4 are characterized by cross laminations showing a seaward paleocurrent direction and have thicknesses of > 35 cm. Almost of their grain-size distributions are similar to the present creek sediments (Fig. 9). From these characteristics of sediments and the present creek topography (~ 1 m wide and 30–50 cm deep), they are considered to be buried channel fills. However, considering the tsunami behavior, such channel-fill deposits could have been formed during a tsunami return-wave period and thus could be either fluvial or tsunami deposits. The grain-size distributions of lower part of SKN-GS4-E6 (Fig. 7) showed similar distribution of present-day beach sediments, indicating the possibility of tsunami return-wave sediments. Other event deposits with a wide grain-size distribution and large amounts of particles both coarser and finer grain sizes than 1−2 phi are more likely to be fluvial instead of tsunami deposits.

Finally, we conducted radiocarbon dating to determine the correlation between tsunami deposits as inferred above and candidates in the GS cores in the incised valley. As a result, we identified five tsunami deposits (TD1–TD5). The modeled ages of each tsunami deposit obtained using OxCal are shown in Table 6 and Additional file 2: Fig. S3. TD1 (500–300 cal yr

**Table 5** Results of radiocarbon dating of samples in SKN-E, SKN-W, and SKN-GS

| Sample no | Lab. no | Location or core name | Sample position | Material | $\delta^{13}C$ [‰] | Conventional $^{14}C$ age [yr BP] | Calibrated age (2σ) [cal BP] | Remark |
|---|---|---|---|---|---|---|---|---|
| 1 | IAAA-181081 | SKN-W | E4/E5 | Organic sediment | − 25.82 ± 0.23 | 424 ± 22 | 520–460 (95.4%) | |
| 2 | IAAA-181082 | SKN-W | E5/B-Tm | Organic sediment | − 30.24 ± 0.20 | 979 ± 22 | 930–890 (33.4%), 880–790 (62.1%) | |
| 3 | IAAA-181805 | SKN-W | B-Tm/E6 | Organic sediment | − 28.44 ± 0.20 | 1315 ± 22 | 1300–1240 (50.5%), 1220–1170 (44.9%) | |
| 4 | IAAA-181083 | SKN-W | E6/E7 | Organic sediment | − 27.41 ± 0.21 | 1357 ± 23 | 1310–1260 (87.0%), 1210–1170 (8.5%) | |
| 5 | IAAA-210212 | SKN-W | below E10 | Plant fragment | − 30.13 ± 0.19 | 1815 ± 24 | 1820–1810 (0.9%), 1800–1760 (4.9%), 1750–1690 (63.7%), 1670–1620 (26.0%) | |
| 6 | IAAA-210213 | SKN-W | below E11 | Organic sediment | − 29.97 ± 0.21 | 2724 ± 24 | 2870–2760 (95.4%) | |
| 7 | IAAA-200962 | SKN-W | below E14 | Organic sediment | − 29.79 ± 0.26 | 3992 ± 26 | 4530–4410 (95.4%) | |
| 8 | IAAA-210214 | SKN-E | below E5 | Organic sediment | − 28.61 ± 0.15 | 3970 ± 27 | 4530–4400 (89.9%), 4370–4350 (2.2%), 4330–4300 (3.3%) | |
| 9 | IAAA-210215 | SKN-E | below E6 | Organic sediment | − 24.25 ± 0.26 | 4320 ± 27 | 4960–4830 (95.4%) | |
| 10 | IAAA-211205 | SKN-E | E11/E12 | Organic sediment | − 26.07 ± 0.23 | 5418 ± 29 | 6290–6180 (93.0%), 6140–6120 (2.5%) | |
| 11 | IAAA-210649 | SKN-GS1 | 58–59 cm in depth | Organic sediment | − 25.92 ± 0.24 | 542 ± 22 | 630–590 (18.0%), 560–520 (77.4%) | |
| 12 | IAAA-210367 | SKN-GS1 | 118–119 cm in depth | Organic sediment | − 25.83 ± 0.19 | 3931 ± 25 | 4510–4490 (2.2%), 4440–4250 (93.2%) | |
| 13 | IAAA-210368 | SKN-GS1 | 141–142 cm in depth | Organic sediment | − 25.39 ± 0.18 | 4209 ± 25 | 4850–4790 (33.3%), 4760–4690 (48.2%), 4680–4640 (14.0%) | |
| 14 | IAAA-210645 | SKN-GS1 | 238–239 cm in depth | Organic sediment | − 26.77 ± 0.24 | 4783 ± 27 | 5590–5470 (95.4%) | |
| 15 | IAAA-210369 | SKN-GS1 | 243.5–244.5 cm in depth | Organic sediment | − 26.72 ± 0.19 | 4902 ± 27 | 5720–5680 (4.5%), 5670–5580 (90.9%) | |
| 16 | IAAA-202305 | SKN-GS2 | 64–65 cm in depth | Organic sediment | − 27.5 ± 0.21 | 1003 ± 21 | 960–900 (78.3%), 870–820 (15.2%), 810–800 (1.9%) | |
| 17 | IAAA-202306 | SKN-GS2 | 70–71 cm in depth | Organic sediment | − 27.32 ± 0.19 | 1239 ± 21 | 1270–1200 (40.0%), 1180–1070 (55.5%) | |
| 18 | IAAA-211211 | SKN-GS2 | 91–92 cm in depth | Organic sediment | − 27.6 ± 0.21 | 2560 ± 24 | 2760–2690 (72.7%), 2640–2610 (7.7%), 2590–2510 (15.0%) | |

**Table 5** (continued)

| Sample no | Lab. no | Location or core name | Sample position | Material | $\delta^{13}C$ [‰] | Conventional $^{14}C$ age [yr BP] | Calibrated age (2σ) [cal BP] | Remark |
|---|---|---|---|---|---|---|---|---|
| 19 | IAAA-210652 | SKN-GS2 | 142–143 cm in depth | Organic sediment | − 29.82 ± 0.23 | 4410 ± 26 | 5260–5250 (0.5%), 5240–5190 (3.7%), 5060–4860 (91.2%) | |
| 20 | IAAA-200960 | SKN-GS2 | 204–206 cm in depth | Organic sediment | − 27.37 ± 0.25 | 4979 ± 28 | 5860–5820 (5.0%), 5750–5600 (90.4%) | |
| 21 | IAAA-211210 | SKN-GS3 | 90–91 cm in depth | Organic sediment | − 26.76 ± 0.22 | 3268 ± 26 | 3570–3440 (90.2%), 3430–3400 (5.3%) | |
| 22 | IAAA-211209 | SKN-GS4 | 97–98 cm in depth | Organic sediment | − 27.1 ± 0.18 | 3405 ± 26 | 3820–3800 (1.0%), 3720–3570 (94.5%) | |
| 23 | IAAA-210651 | SKN-GS5 | 63–64 cm in depth | Organic sediment | − 27.1 ± 0.25 | 4005 ± 25 | 4530–4410 (95.4%) | |
| 24 | IAAA-202304 | SKN-GS5 | 171–172 cm in depth | Organic sediment | − 22.62 ± 0.19 | 6673 ± 29 | 7610–7470 (95.4%) | |
| 25 | IAAA-210217 | SKN-GS6 | 44–45 cm in depth | Organic sediment | − 28.52 ± 0.27 | 268 ± 21 | 430–370 (28.6%), 330–280 (62.3%), 170–150 (4.5%) | |
| 26 | IAAA-210365 | SKN-GS6 | 57–58 cm in depth | Organic sediment | − 28.87 ± 0.19 | 615 ± 21 | 650–550 (95.4%) | |
| 27 | IAAA-211208 | SKN-GS6 | 96–97 cm in depth | Organic sediment | − 25.6 ± 0.22 | 2782 ± 25 | 2960–2840 (81.4%), 2830–2780 (14.0%) | |
| 28 | IAAA-210650 | SKN-GS6 | 132–133 cm in depth | Organic sediment | − 27.9 ± 0.22 | 4160 ± 25 | 4830–4580 (95.4%) | |
| 29 | IAAA-210366 | SKN-GS6 | 134–135 cm in depth | Organic sediment | − 25.77 ± 0.18 | 4125 ± 25 | 4820–4750 (28.1%), 4730–4520 (67.3%) | |
| 30 | IAAA-210646 | SKN-GS6 | 151–152 cm in depth | Organic sediment | − 27.2 ± 0.23 | 4457 ± 26 | 5290–5160 (47.3%), 5140–4960 (48.1%) | |
| 31 | IAAA-210218 | SKN-GS6 | 165–166 cm in depth | Organic sediment | − 30.01 ± 0.20 | 4643 ± 28 | 5470–5310 (95.4%) | |
| 32 | IAAA-210219 | SKN-GS6 | 173–174 cm in depth | Organic sediment | − 27.84 ± 0.19 | 5102 ± 29 | 5920–5840 (36.2%), 5830–5740 (59.2%) | |
| 33 | IAAA-210220 | SKN-GS6 | 195–196 cm in depth | Organic sediment | − 28.69 ± 0.18 | 5099 ± 29 | 5920–5840 (35.7%), 5830–5740 (59.8%) | |
| 34 | IAAA-210221 | SKN-GS6 | 228.5–229.5 cm in depth | Organic sediment | − 29.06 ± 0.18 | 5211 ± 29 | 6110–6080 (5.5%), 6010–5900 (89.9%) | |
| 35 | IAAA-200961 | SKN-GS6 | 262–264 cm in depth | Organic sediment | − 26.88 ± 0.25 | 5524 ± 28 | 6400–6280 (95.4%) | |
| 36 | IAAA-210643 | SKN-GS7 | 40–41 cm in depth | Organic sediment | − 25.69 ± 0.21 | 555 ± 21 | 630–590 (36.7%), 560–520 (58.8%) | |
| 37 | IAAA-210644 | SKN-GS8 | 74–75 cm in depth | Organic sediment | − 26.9 ± 0.21 | 503 ± 21 | 550–500 (95.4%) | |
| 38 | IAAA-210216 | SKN-GS9 | 62–63 cm in depth | Organic sediment | − 27.8 ± 0.21 | 412 ± 22 | 520–450 (90.5%), 360–330 (4.9%) | |
| 39 | IAAA-211206 | SKN-GS9 | 118–119 cm in depth | Organic sediment | − 25.2 ± 0.22 | 3264 ± 25 | 3570–3440 (87.6%), 3430–3400 (7.8%) | |

**Table 5** (continued)

| Sample no | Lab. no | Location or core name | Sample position | Material | δ$^{13}$C [‰] | Conventional $^{14}$C age [yr BP] | Calibrated age (2σ) [cal BP] | Remark |
|---|---|---|---|---|---|---|---|---|
| 40 | IAAA-211207 | SKN-GS9 | 165–166 cm in depth | Organic sediment | − 25.2 ± 0.21 | 3940 ± 26 | 4520–4480 (8.8%), 4450–4290 (85.3%), 4270–4250 (1.4%) | |
| 41 | IAAA-210647 | SKN-GS9 | 175–176 cm in depth | Organic sediment | − 27.9 ± 0.24 | 4017 ± 26 | 4570–4550 (1.2%), 4530–4410 (94.2%) | |
| 42 | IAAA-210648 | SKN-GS9 | 201–202 cm in depth | Organic sediment | − 29.5 ± 0.24 | 4350 ± 27 | 5030–5010 (1.3%), 4980–4850 (94.1%) | |
| 43 | IAAA-181806 | SKN-E | below U-2 drift pumice | Organic sediment | − 22.9 ± 0.21 | 4710 ± 30 | 5580–5500 (17.2%), 5490–5430 (23.9%), 5420–5320 (54.4%) | Hiramine et al. (in press) |
| 44 | IAAA-181607 | SKN-E | below To-Cu ash | Organic sediment | − 24.6 ± 0.39 | 5180 ± 30 | 6000–5900 (95.4%) | Ishimura and Hiramine (2020) |
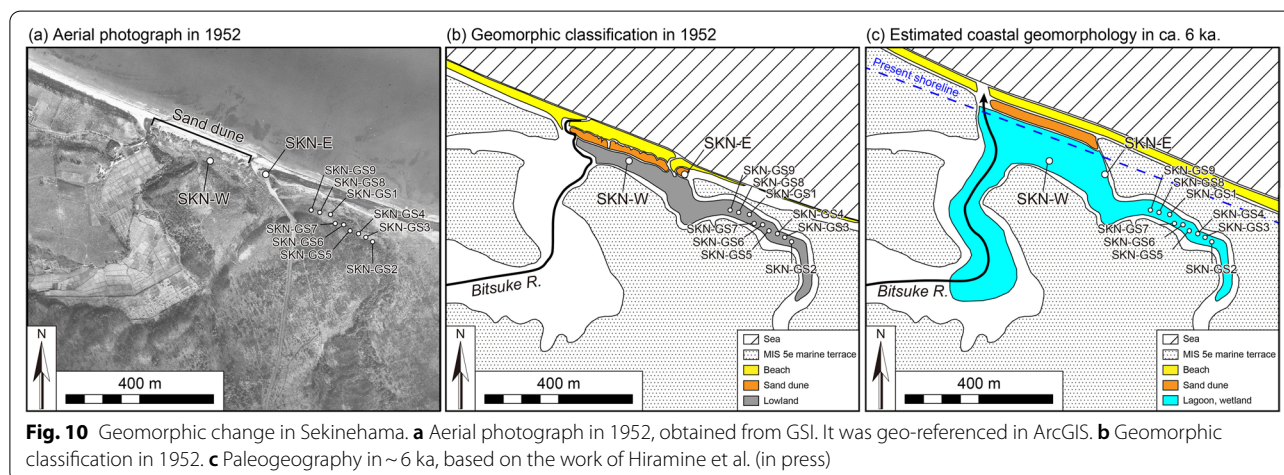


**Fig. 10** Geomorphic change in Sekinehama. **a** Aerial photograph in 1952, obtained from GSI. It was geo-referenced in ArcGIS. **b** Geomorphic classification in 1952. **c** Paleogeography in ~6 ka, based on the work of Hiramine et al. (in press)

BP (1450–1650 cal CE)) is the latest tsunami deposit (E1 deposit in all cores) in this study and is distributed above B-Tm tephra. TD1 in many of the cores shows a grain-size distribution similar to that of the beach sediments, with multiple units and thinning inland. TD2 (4490–4300 cal yr BP; SKN-GS1-E2, SKN-GS8-E2, and SKN-GS9-E3), found up to SKN-GS1 and not farther inland, shows a grain-size distribution similar to that of the beach sediments, with an erosive contact at the base in SKN-GS1. TD3 (4790–4580 cal yr BP; SKN-GS1-E3, SKN-GS6-E2, SKN-GS8-E3, and SKN-GS9-E4) shows a grain-size distribution similar to that of the beach sediments, with an erosive contact at the base in SKN-GS1. The sedimentary structure of SKN-GS1-E3 shows a paleocurrent direction inland. SKN-GS7-E3 was a channel-fill

deposit that may have been formed by the return wave during the TD3 deposition. TD4 (5420–5030 cal yr BP; SKN-GS2-E2 and SKN-GS6-E3) has a slightly finer-grain-size distribution in the beach sediments. In SKN-GS6-E3, the paleocurrent direction inland was estimated from the sedimentary structure. SKN-GS1-E4 and SKN-GS8-E4 were channel-fill deposits and may have been formed by the return wave during TD4 deposition. TD5 (6030–5790 cal yr BP; SKN-GS1-E5, SKN-GS2-E5, SKN-GS6-E6, and SKN-GS8-E5) shows a grain-size distribution similar to that of the beach sediments, with an erosive contact at the base. The sedimentary structure of SKN-GS6-E6 shows a paleocurrent direction inland. SKN-GS4-E6 was channel-fill deposit and may have been formed by the return wave during TD5 deposition. In the
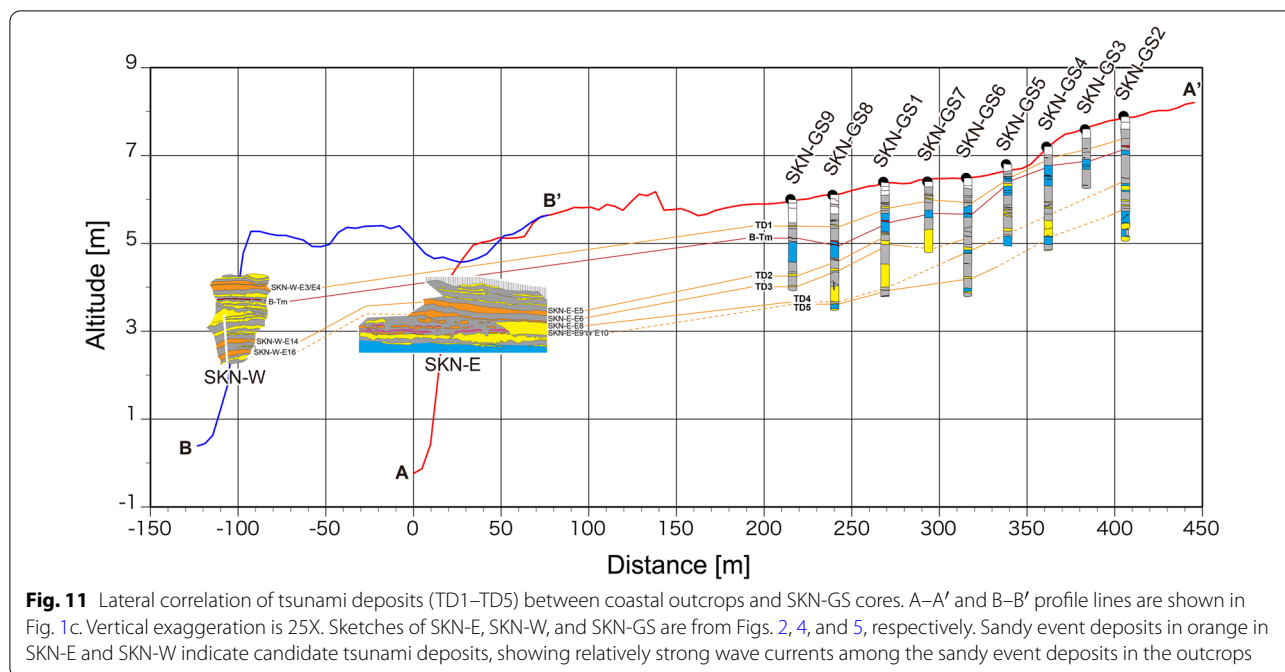
**Fig. 11** Lateral correlation of tsunami deposits (TD1–TD5) between coastal outcrops and SKN-GS cores. A–A′ and B–B′ profile lines are shown in Fig. 1c. Vertical exaggeration is 25X. Sketches of SKN-E, SKN-W, and SKN-GS are from Figs. 2, 4, and 5, respectively. Sandy event deposits in orange in SKN-E and SKN-W indicate candidate tsunami deposits, showing relatively strong wave currents among the sandy event deposits in the outcrops

**Table 6** Modeled ages of TD1–TD5

| Tsunami deposits | Modeled age (cal yr BP) |
|---|---|
| TD1 | 500–300 (1450–1650 cal CE) |
| TD2 | 4490–4300 |
| TD3 | 4790–4580 |
| TD4 | 5420–5030 |
| TD5 | 6030–5790 |

ITRAX results (Fig. 8), some sand layers (e.g., SKN-GS1-E3 and SKN-GS6-E6) show an increase in S, which is an indicator of marine intrusion (e.g., Chagué-Goff et al. 2016), supporting the above identifications of tsunami deposits.

In addition, SKN-GS1-E6, SKN-GS6-E7, and SKN-GS8-E6 may be correlated. SKN-GS6-E7 shows a finer-grain-size distribution than that of the beach sediments, while SKN-GS1-E6 and SKN-GS8-E6 show grain-size distributions similar to those of the beach sediments. The ITRAX results show a slight increase in S at SKN-GS1-E6 (Fig. 8). However, because they are near the base of the cores, and the underlying sediments were not fully observable, they are not identified here as tsunami deposits.

### 5.5 Interpretation of event deposits in SKN-E and SKN-W outcrops

Candidates for tsunami deposits in SKN-W are SKN-W-E3/E4, SKN-W-E10, SKN-W-E11, and SKN-W-E14

because all of them have erosional contacts at the base and are distinct sand layers compared to the other event deposits (Table 2). In contrast, SKN-W-E1 and SKN-W-E8 characteristically exhibit thicker layers and parallel laminae. These features are commonly observed in washover deposits caused by storm surges behind the coast (e.g., Morton et al. 2007). Additionally, SKN-W-E1 is distributed up to the ground surface (Fig. 4). Considering the most recent topographic changes (Fig. 10a, b), it could be a washover deposit formed by a storm surge that eroded the coastal sand dune in the past 50 years. In SKN-E, SKN-E-E5, SKN-E-E6, and SKN-E-E8 are candidates for tsunami deposits because all of them have erosive contact at the base with rip-up clasts. The rip-up clast is often used as one of the indicators for identifying tsunami deposits (e.g., Goff et al. 2012) and for distinguishing tsunami and storm-surge deposits (e.g., Kortekaas and Dawson 2007). SKN-E-E5 in particular includes a few centimeters of gravels and pumice clasts, suggesting a stronger flow compared to other event deposits in the outcrop. SKN-E-E7 is a channel-fill deposit with parallel laminae. Taking into account the paleogeography (Fig. 10c), it could be fluvial sediments that buried the creek flowing through the wetland or tidal-channel sediments that filled the channel connecting to the sea.

To correlate the sediments between the two outcrops, we used radiocarbon dating on deposits below the tsunami-deposit candidates mentioned above, which are expected to be widely distributed in the study area. Dates

for samples collected below SKN-E-E5 and SKN-W-E14 are $3970 \pm 27$ yr BP and $3992 \pm 26$ yr BP, respectively. This coincidence means that they are the sandy deposits related to the same event. These dates added to the tephra ages and other radiocarbon dates confirmed having continuous sediments from the present to 6300 cal yr BP exposed in the outcrops.

Grain-size analyses of the outcrop samples show that almost all the event deposits have a mode at 1–2 phi, similar to the present-day beach (Figs. 3, 9). In the SKN-E outcrop, SKN-E-E1 to SKN-E-E4 (younger than ~ 4500 cal yr BP) show a narrow grain-size distribution with a 1–2-phi mode. In contrast, SKN-E-E5 to SKN-E-E10 (4500–6000 cal yr BP) exhibit 1–2-phi modes but wider grain-size distributions. Below SKN-E-E11 (older than ~ 6000 cal yr BP), the mode shifts to a somewhat-smaller size (2 phi), and the proportion of fine-grained particles increases. A similar trend of grain-size variation was observed in the SKN-W outcrop. From SKN-W-E1 to SKN-W-E13 (present to 4500 cal yr BP), they show narrow grain-size distributions with 1–2-phi modes. SKN-W-E14 to SKN-W-E16 (older than 4500 cal yr BP) show 1–2-phi modes but with wider grain-size distributions. SKN-W-E17 has a smaller mode (2 phi) and contains a higher proportion of fine-grained particles compared to the event deposits above it. This similarity in the grain-size distribution of the event deposits at the two sites according to age suggests the existence of common event deposits at the two sites. However, the numbers of event deposits between the two sites do not necessarily match, and correlations with radiocarbon dates are difficult because of the close distributions of event deposits. In Sect. 5.6, we correlate the tsunami deposits (TD1–TD5) identified in the SKN-GS cores to the event deposits in these outcrops.

### 5.6 Tsunami deposits distribution in Sekinehama
From the dating results, we correlated tsunami-deposit candidates among the coastal outcrops to TD1–TD5 in the GS cores (Figs. 2, 4, 11). TD1 correlates with SKN-W-E3/E4, which has an erosional base, and was traced in the SKN-W-GS cores drilled behind the outcrop. In outcrop, they present as two separate units, indicating the multiple waves. This feature is consistent with the sedimentary facies of E1 deposits of the SKN-GS cores. Accordingly, TD1 was deposited by a tsunami with multiple waves during 500–300 cal yr BP (1450–1650 cal CE).

TD2, TD3, and TD4 were correlated with SKN-E-E5, SKN-E-E6, and SKN-E-E8, respectively. Because these three layers have coarse grains, an erosional base, and rip-up clasts, we consider them to have been deposited by strong wave currents. Considering the radiocarbon dates, TD5 may correlate with SKN-E-E9 or SKN-E-E10.

In SKN-W, we correlated SKN-W-E14 to TD2. SKN-W-E16 may correspond to TD3, but the age could not be measured owing to the low organic carbon content. Considering the age of the sediments, it is unlikely that TD4 and TD5 are represented in SKN-W.

These results allowed us to correlate tsunami deposits from the coastal outcrops to deposits 200–400 m inland (Fig. 11). These distributions also indicate that TD1–TD5 were deposited by large tsunamis compared to historical tsunamis (Table 1). TD1, TD4, and TD5 are distributed the farthest inland among the five tsunami deposits. However, the fact that the sediments in the coastal outcrops were deposited in lowlands behind dunes and that the other event deposits not correlated with TD1–TD5 show similar grain-size distributions with those of the beach sediments suggests that they may have been deposited by smaller tsunamis or by low-frequency storm-surge events. This is consistent with our interpretation that the thick event deposits with multiple laminations and limited distributions (SKN-W-E1 and SKN-W-E8) are washover deposits associated with storm surges.

Between TD2 and B-Tm tephra, multiple event deposits are commonly recognized in the coastal outcrops, whereas no distinct event deposits are recognized between them in the GS cores. The GS cores yield dates of ~ 3000 cal yr BP ~ 50 cm below the B-Tm tephra. The sedimentary facies show no unconformity below B-Tm, but this indicates that the sedimentation rate was low or it represents a hiatus. Given the absence of event deposits between TD2 and B-Tm tephra in the GS core, apparently event deposits either are distributed only near the coast or are not well preserved in the GS cores.

### 5.7 Tsunami deposits correlation in Tohoku and Hokkaido regions
Considering the correlation to more-distant tsunami deposits, TD1 (500–300 cal yr BP (1450–1650 cal CE)) can be correlated with the 1611 Keicho tsunami deposits on the Sanriku Coast, the seventeenth-century tsunami deposits in western Hokkaido, and the 1640 Komagatake tsunami deposits. The 1454 Kyotoku tsunami (Namegaya and Yata 2014) also appeared to be a possible correlative event linked to TD1, but Ishizawa et al. (2022) showed that there is no deposit from the 1454 Kyotoku tsunami on the northern Sanriku Coast (Fig. 1a). As for the 1640 Komagatake tsunami, numerical simulations conducted by Nakanishi and Okamura (2019) to explain the tsunami-deposit distributions show that with distance from the source the wave heights decreased. As Sekinehama is ~ 100 km from the Komagatake, the calculated tsunami height was < 5 m, which is below the present sea-cliff height of ~ 5 m (Fig. 11), meaning that the 1640 Komagatake tsunami likely did not inundate the locations of the

studied GS cores. Also, Sato et al. (in press in this special issue) confirmed that the simulated 1640 Komagatake tsunami would not have inundated the GS core sites in our study.

To explain the tsunami deposits near the study site (Minoura et al. 2013; Tanigawa et al. 2014; Kase et al. 2022; Fig. 1), it was necessary to assume the occurrence of an unknown tsunami in the fifteenth century, considering that only one layer of tsunami deposits at each site has been identified during the last 1500 years (Fig. 12), the topographical settings (distance from the coastline and elevation) of each site, and the uncertainties of ages due to differences in dating materials. We determined the depositional ages of the latest tsunami deposits within a 50-km distance from Sekinehama (Figs. 1, 12) to be as

follows: Ta1 deposit (589–516 cal yr BP (1361–1434 cal CE)) at the Takadai-cho site in Hokkaido (Elevation is 6.4 m, and distance from the coast is 200 m; Kase et al. 2022), TD1 (500–300 cal yr BP (1450–1650 cal CE)) in this study (Elevation is ~5–7 m, and distance from the coast is ~200–400 m), a tsunami deposit (681–490 cal yr BP (1269–1460 cal CE)) on the east coast of Shimokita Peninsula (Elevation is ~21–22 m, and distance from the coast is ~1350 m; Minoura et al. 2013), and S1 deposit (470–180 cal yr BP (1480–1770 cal CE)) on the east coast of Shimokita Peninsula (Elevation is ~3–5.5 m, and distance from the coast is ~700–1050 m; Tanigawa et al. 2014.). Although not completely overlapping, they are very close to the mid-fifteenth century (Fig. 12). If they were all deposited by the same tsunami event, we
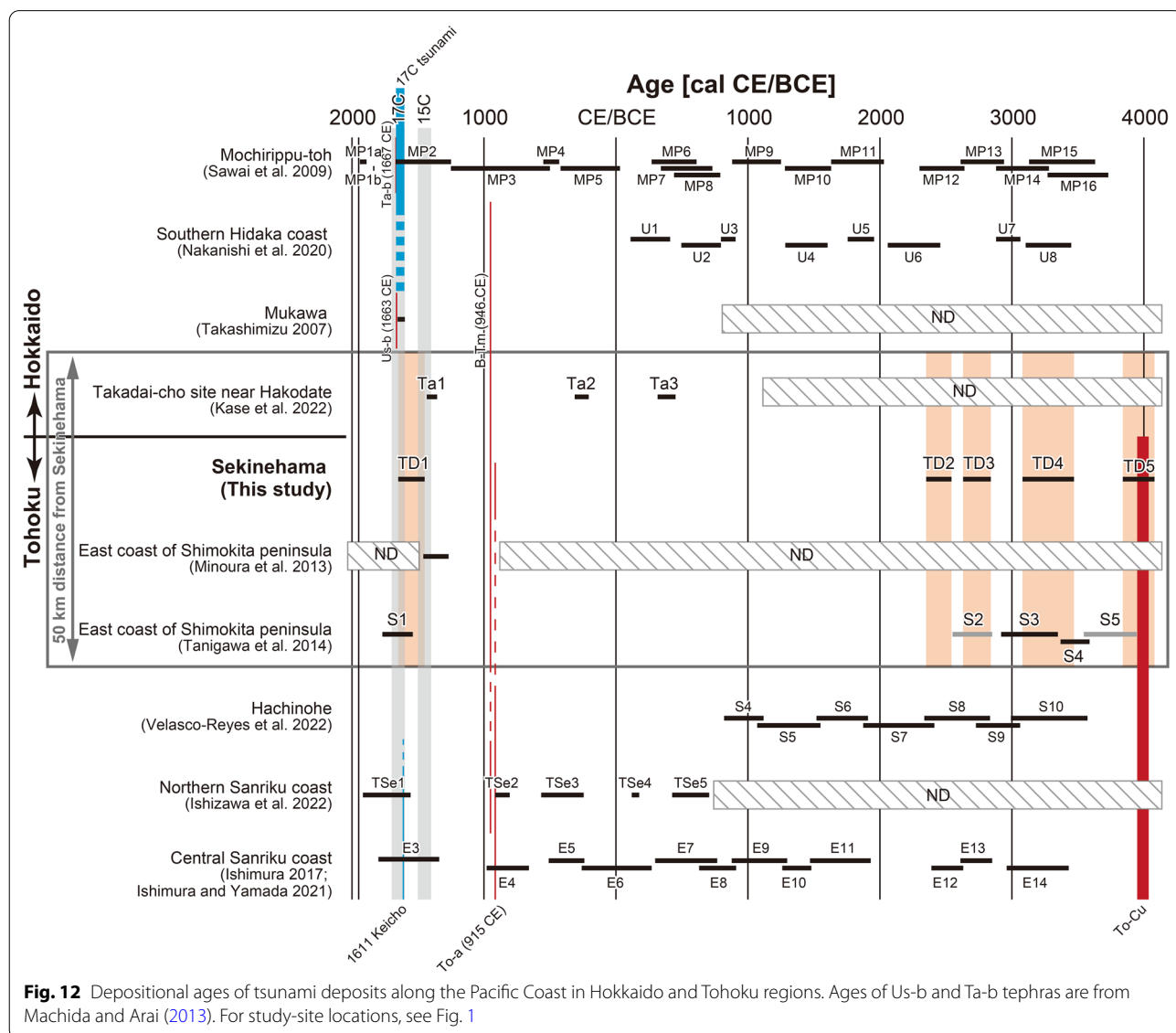


**Fig. 12** Depositional ages of tsunami deposits along the Pacific Coast in Hokkaido and Tohoku regions. Ages of Us-b and Ta-b tephras are from Machida and Arai (2013). For study-site locations, see Fig. 1

Ishimura *et al. Progress in Earth and Planetary Science* (2022) 9:69

Page 24 of 27

assume they were deposited in the mid-fifteenth century. Accordingly, and given the seventeenth-century tsunami in Hokkaido and the 1611 Keicho tsunami on the Sanriku Coast, the latest tsunami deposits at Sekinehama could have been deposited by an indeterminate fifteenth-century tsunami that has yet to be recognized in the historical record.

We correlated TD2–TD5 to tsunami deposits identified near the Sekinehama Coast. On the other side of the Tsugaru Strait, in addition to Ta1 mentioned above, Kase et al. (2022) identified two tsunami deposits (Ta2 and Ta3) at the Takadai-cho site (Fig. 1a), which is the closest to our study site among their study sites. The ages of Ta2 and Ta3 are 1745–1639 cal yr BP and 2401–2265 cal yr BP, respectively (Fig. 12). Although they do not correlate with TD2–TD5, radiocarbon dates indicate that they may correlate with SKN-W-E7 to SKN-W-E10. However, Kase et al. (2022) stated that the areal distributions of Ta1–Ta3 were not confirmed and were limited to a narrow area of 10 m or less. Therefore, more excavation and drilling surveys similar to our current study are needed to confirm the inland distribution and correlate laterally.

In addition to the already-described S1, Tanigawa et al. (2014) identified four sandy event deposits (S2–S5) that formed during the last 6000 years and concluded that S1, S3, and S4 were deposited by seawater inundation on the basis of diatom analysis. The ages of the four deposits are as follows (Fig. 12): S2 (4800–4500 cal yr BP), S3 (5300–4870 cal yr BP), S4 (5540–5320 cal yr BP), and S5 (5890–5490 cal yr BP). We correlated TD4 (5420–5030 cal yr BP) to S3 or S4. If S2 and S5 are also tsunami deposits, we would correlate TD3 (4790–4580 cal yr BP) to S2 and TD5 (6030–5790 cal yr BP) to S5. Tanigawa et al. (2014) also found no seawater inundation over a long period between S1 and S2 or S3. Thus, the depositional ages and intervals that they determined for the tsunami deposits are similar to those in our study. In addition, S1 and S3 are distributed farthest inland in the drilling area, which is also consistent with the distribution of TD1 and TD4 in our study (Fig. 11).

We also investigated correlation to deposits in more-distant areas. West of the Hidaka Coast in Hokkaido, tsunami deposit during 4000–6000 cal yr BP is unknown (Takashimizu, 2014). In the southern Hidaka Coast area, dates for tsunami deposits that formed during 5.5–2.2 ka were obtained by Nakanishi et al. (2020): U1: 2360–2060 cal yr BP, U2: 2745–2445 cal yr BP, U3: 2856–2745 cal yr BP, U4: 3553–3233 cal yr BP, U5: 3905–3705 cal yr BP, U6: 4407–4009 cal yr BP, U7: 5014–4830 cal yr BP, and U8: 5399–5054 cal yr BP (Fig. 12). Although tsunami deposits that correlate with our results are distributed, Nakanishi et al. (2021) considered that their tsunami sources were likely to be along the Kuril

Trench (Fig. 1a). Therefore, to confirm correlation, tsunami sources need to be addressed. Similarly, although TD2–TD5 could be correlated with tsunami deposits identified along the Sanriku Coast (Fig. 12; Ishimura 2017; Ishimura and Yamada 2021; Ishizawa et al. 2022; Velasco-Reyes et al., 2022), we need to assess whether tsunamis off the Sanriku Coast could generate tsunamis inundating Sekinehama. Thus, although there is a possibility that the tsunami deposits in Sekinehama correlate with those in the Hokkaido and the Sanriku Coast, further investigation involving tsunami sources is needed to correlate the Sekinehama deposits to more-distant tsunami deposits.

## 6 Conclusions

In this study, we performed nondestructive analyses (XCT and ITRAX μXRF core scanning), grain-size analysis, tephra analysis, and radiocarbon dating of sediments exposed in the two coastal outcrops and GS cores at Sekinehama on the north coast of the Shimokita Peninsula, which is near the junction of the Japan and Kuril trenches. By comparing grain-size distribution between sandy event deposits and present-day source sediments and by investigating detailed sedimentary structures observed in XCT images, we found that some event deposits show transportation inward from the coast. Finally, we identified five tsunami deposits (TD1–TD5) that formed since ∼ 6 ka and correlated them from coastal outcrops to the incised valley based on radiocarbon dating and tephrochronology. We also found that other washover deposits were among the coastal outcrops but not in the GS cores. This limited distribution indicates minor washover events related to small tsunamis and low-frequency storm surges.

The modeled age of the latest tsunami deposit is 500–300 cal yr BP (1450–1650 cal CE). This may be correlative with two known tsunamis (seventeenth-century tsunami in Hokkaido and 1611 Keicho tsunami in Tohoku) or may be an unknown tsunami that possibly occurred during the fifteenth–seventeenth centuries. If the latest tsunami deposit is correlated with either or both of the seventeenth-century and 1611 Keicho tsunamis, the tsunami inundation area would be expanded, resulting in the need for a complex tsunami source model. However, if the latest tsunami deposit is correlated with tsunami deposits previously identified within a 50-km distance from the study site, we need to consider an unknown fifteenth-century tsunami and use a different source model set off the Shimokita Peninsula. Nonetheless, our determination of the latest tsunami deposit is one constraint with high reliability for constraining the tsunami source models in the future even if not correlated with any specific tsunamis.

Ishimura *et al. Progress in Earth and Planetary Science*        (2022) 9:69

Page 25 of 27

To tackle possible simultaneity and the as-yet-indeterminate source of the seventeenth-century tsunami in the Hokkaido region and the 1611 Keicho tsunami in the Tohoku region, we need to conduct tsunami-deposit surveys in other areas along the Pacific Coast near the junction of the Japan and Kuril trenches. The tsunami deposits TD2–TD5 could be correlated with those on the east coast of the Shimokita Peninsula by their depositional ages. To correlate with more-distant tsunami deposits in the Hokkaido and Tohoku regions, tsunami sources need to be assessed because there are many correlative tsunami deposits in those regions.

## Abbreviations

cps: Counts per second; DEM: Digital elevation model; GSI: Geospatial Information Authority of Japan; TD: Tsunami deposits; XCT: X-ray computed tomography; μXRF: Micro-X-ray-fluorescence.

## Supplementary Information

The online version contains supplementary material available at https://doi.org/10.1186/s40645-022-00529-9.

---

**Additional file 1.** OxCal code.

**Additional file 2. Supplementary figures and table. Fig. S1a.** Results of the ITRAX micro-X-ray fluorescence core scanning of SKNGS9. Each elemental datum was normalized by counts per second (cps). **Fig. S1b.** Results of the ITRAX micro-Xray fluorescence core scanning of SKN-GS5. Each elemental datum was normalized by counts per second (cps). **Fig. S1c.** Results of the ITRAX micro-X-ray fluorescence core scanning of SKN-GS4. Each elemental datum was normalized by counts per second (cps). **Fig. S1d.** Results of the ITRAX micro-X-ray fluorescence core scanning of SKN-GS2. Each elemental datum was normalized by counts per second (cps). **Fig. S2.** Major element compositions of volcanic glass shards. **Fig. S3.** OxCal output of TD1 to TD5. We performed OxCal modeling using the Sequence model (Bronk Ramsey, 2008). **Table S1.** Results of grain analysis.

---

## Author contributions

DI designed this research, conducted tephra and grain analyses, and drafted the manuscript. All authors conducted the GS drilling survey. MY and TI discussed the sedimentary features of event deposits. TI checked the age modeling with OxCal. KA conducted tephra analysis in SKN-W and discussed the tephra correlation. KS compiled information on the tsunami-deposit research and tsunami source modeling. All authors read and approved the final manuscript.

## Availability of data and materials

The datasets supporting the conclusions of this article are included within the article and its additional files.

### Author details

[1]Department of Geography, Tokyo Metropolitan University, 1-1 Minami-Osawa, Hachioji, Tokyo 192-0397, Japan. [2]International Research Institute of Disaster Science, Tohoku University, 468-1 Aoba, Aramaki, Aoba-ku, Sendai, Miyagi 980-8572, Japan. [3]Department of Geology, Faculty of Science, Shinshu University, 3-1-1 Asahi, Matsumoto, Nagano 390-8621, Japan. [4]Research Center for Volcanic Hazards and Their Mitigation, Tokyo Metropolitan University, 1-1 Minami-Osawa, Hachioji, Tokyo 192-0397, Japan. [5]Department of Earth and Planetary Science, The University of Tokyo, 7-3-1 Hongo, Bunkyo-ku, Tokyo 113-0033, Japan.

## References

Bronk Ramsey C (2008) Deposition models for chronological records. Quat Sci Rev 27:42–60. https://doi.org/10.1016/j.quascirev.2007.01.019

Bronk Ramsey C (2009) Bayesian analysis of radiocarbon dates. Radiocarbon 51:337–360. https://doi.org/10.2458/azu_js_rc.v51i1.3494

Chagué-Goff C, Chan JCH, Goff J, Gadd P (2016) Late Holocene record of environmental changes, cyclones and tsunamis in a coastal lake, Mangaia, Cook Islands. Isl Arc 25:333–349. https://doi.org/10.1111/iar.12153

Costa PJM, Andrade C (2020) Tsunami deposits: present knowledge and future challenges. Sedimentology 67:1189–1206. https://doi.org/10.1111/sed.12724

Croudace IW, Rindby A, Rothwell RG (2006) ITRAX: description and evaluation of a new multi-function X-ray core scanner. Geol Soc Spec Publ 267:51–63. https://doi.org/10.1144/GSL.SP.2006.267.01.04

Davies SJ, Lamb HF, Roberts SJ (2015) Micro-XRF core scanning in palaeolimnology: recent developments. In: Croudace IW, Rothwell RG (eds) Micro-XRF studies of sediment cores, developments in paleoenvironmental research, vol 17. Springer, Dordrecht, pp 189–226. https://doi.org/10.1007/978-94-017-9849-5_7

Ebina Y, Imai K (2014) Tsunami traces survey of the 1611 Keicho Ohsyu earthquake tsunami based on historical documents and traditions. Rep Tsunami Eng 31:139–148 (**in Japanese**)

Falvard S, Paris R (2017) X-ray tomography of tsunami deposits: towards a new depositional model of tsunami deposits. Sedimentology 64:453–477. https://doi.org/10.1111/sed.12310

Goff J, Chagué-Goff C, Nichol S, Jaffe B, Dominey-Howes D (2012) Progress in palaeotsunami research. Sediment Geol 243–244:70–88. https://doi.org/10.1016/j.sedgeo.2011.11.002

Goto K, Ikehara K, Goff J, Chagué-Goff C, Jaffe B (2014) The 2011 Tohoku-oki tsunami—three years on. Mar Geol 358:2–11. https://doi.org/10.1016/j.margeo.2014.08.008

Goto T, Satake K, Sugai T, Ishibe T, Harada T, Murotani S (2015) Historical tsunami and storm deposits during the last five centuries on the Sanriku coast, Japan. Mar Geol 367:105–117. https://doi.org/10.1016/j.margeo.2015.05.009

Goto K, Ishizawa T, Ebina Y, Imamura F, Sato S, Udo K (2021) Ten years after the 2011 Tohoku-oki earthquake and tsunami: geological and environmental effects and implications for disaster policy changes. Earth Sci Rev 212:103417. https://doi.org/10.1016/j.earscirev.2020.103417

Hiramine R, Aoki K, Ishimura D (in press) Holocene drift pumices and their source volcanoes at Sekinehama, Mutsu city, Aomori prefecture, Japan. Quat Res. **(in Japanese)**

Inoue T, Goto K, Nishimura Y, Watanabe M, Iijima Y, Sugawara D (2017) Paleotsunami history along the northern Japan Trench: evidence from Noda Village, northern Sanriku coast, Japan. Prog Earth Planet Sci 4:1–15. https://doi.org/10.1186/s40645-017-0158-1

Ioki K, Tanioka Y (2016) Re-estimated fault model of the 17th century great earthquake off Hokkaido using tsunami deposit data. Earth Planet Sci Lett 433:133–138. https://doi.org/10.1016/j.epsl.2015.10.009

Ishimura *et al. Progress in Earth and Planetary Science*　　　(2022) 9:69

Page 26 of 27

Ishimura D (2017) Re-examination of the age of historical and paleo-tsunami deposits at Koyadori on the Sanriku Coast, Northeast Japan. Geosci Lett 4:11. https://doi.org/10.1186/s40562-017-0077-4

Ishimura D, Ebina Y (2021) Historical and geological examination of the tradition at the watershed between Koyadori and Oura, Yamada town, Iwate prefecture. Hist Earthq 36:89–97 (**in Japanese with English abstract**)

Ishimura D, Hiramine R (2020) Proximal–distal fall deposit correlation of VEI-5 tephra (Towada-Chuseri) from Towada volcano, northeast Japan. J Quat Sci 35:334–348. https://doi.org/10.1002/jqs.3161

Ishimura D, Miyauchi T (2015) Historical and paleo-tsunami deposits during the last 4000 years and their correlations with historical tsunami events in Koyadori on the Sanriku Coast, northeastern Japan. Prog Earth Planet Sci 2:16. https://doi.org/10.1186/s40645-015-0047-4

Ishimura D, Miyauchi T (2017) Holocene environmental changes and paleo-tsunami history in Onuma on the southern part of the Sanriku Coast, northeast Japan. Mar Geol 386:126–139. https://doi.org/10.1016/j.margeo.2017.01.011

Ishimura D, Yamada K (2019) Palaeo-tsunami inundation distances deduced from roundness of gravel particles in tsunami deposits. Sci Rep 9:10251. https://doi.org/10.1038/s41598-019-46584-z

Ishimura D, Yamada K (2021) Integrated lateral correlation of tsunami deposits during the last 6000 years using multiple indicators at Koyadori, Sanriku Coast, northeast Japan. Quat Sci Rev 256:106834. https://doi.org/10.1016/j.quascirev.2021.106834

Ishizawa T, Goto K, Yokoyama Y, Miyairi Y (2019) Non-destructive analyses to determine appropriate stratigraphic level for dating of tsunami deposits. Mar Geol 412:19–26. https://doi.org/10.1016/j.margeo.2019.02.009

Ishizawa T, Goto K, Yokoyama Y, Miyairi Y, Sawada C, Nishimura Y, Sugawara D (2017) Sequential radiocarbon measurement of bulk peat for high-precision dating of tsunami deposits. Quat Geochronol 41:202–210. https://doi.org/10.1016/j.quageo.2017.05.003

Ishizawa T, Goto K, Nishimura Y, Miyairi Y, Sawada C, Yokoyama Y (2022) Paleotsunami history along the northern Japan trench based on sequential dating of the continuous geological record potentially inundated only by large tsunamis. Quat Sci Rev 279:107381. https://doi.org/10.1016/j.quascirev.2022.107381

Kase Y, Kawakami G, Koyasu H, Takahashi R, Sagayama T, Nishina K (2022) Event deposits recognized in the lowlands along the Tsugaru Strait, Hokkaido, Japan. J Geol Soc Jpn 128:7–26 (**in Japanese with English abstract**)

Kortekaas S, Dawson AG (2007) Distinguishing tsunami and storm deposits: an example from Martinhal, SW Portugal. Sediment Geol 200:208–221. https://doi.org/10.1016/j.sedgeo.2007.01.004

Kobayashi M (2019) Volcanic ejecta as indicators for formations of coastal sediments in the northern Shimokita Peninsula. Report for grant of Shimokita geopark **(in Japanaese)**

Koike K, Machida H (2001) Atlas of quaternary marine terraces in the Japanese islands. University of Tokyo Press, Tokyo (**in Japanese**)

Löwemark L, Chen HF, Yang TN, Kylander M, Yu EF, Hsu YW, Lee TQ, Song SR, Jarvis S (2011) Normalizing XRF-scanner data: a cautionary note on the interpretation of high-resolution records from organic-rich lakes. J Asian Earth Sci 40:1250–1256. https://doi.org/10.1016/j.jseaes.2010.06.002

Machida H, Arai F (2013) Atlas of tephra in and around Japan [revised edition]. University of Tokyo Press, Tokyo (**in Japanese**)

Martin-Puertas C, Tjallingii R, Bloemsma M, Brauer A (2017) Varved sediment responses to early Holocene climate and environmental changes in Lake Meerfelder Maar (Germany) obtained from multivariate analyses of micro X-ray fluorescence core scanning data. J Quat Sci 32:427–436. https://doi.org/10.1002/jqs.2935

McLean D, Albert PG, Nakagawa T, Suzuki T, Staff RA, Yamada K, Kitaba I, Haraguchi T, Kitagawa J, SG14 Project Members, Smith VC (2018) Integrating the Holocene tephrostratigraphy for East Asia using a high-resolution cryptotephra study from Lake Suigetsu (SG14 core), central Japan. Quat Sci Rev 183:36–58. https://doi.org/10.1016/j.quascirev.2017.12.013

Minoura K, Hirano S, Yamada T (2013) Identification and possible recurrence of an oversized tsunami on the Pacific coast of northern Japan. Nat Hazards 68:631–643. https://doi.org/10.1007/s11069-013-0640-z

Mitra R, Naruse H, Abe T (2020) Estimation of tsunami characteristics from deposits: inverse modeling using a deep-learning neural network. J Geophys Res Earth Surf 125:1–22. https://doi.org/10.1029/2020JF005583

Mitra R, Naruse H, Fujino S (2021) Reconstruction of flow conditions from 2004 Indian Ocean tsunami deposits at the Phra Thong island using a deep neural network inverse model. Nat Hazards Earth Syst Sci 21:1667–1683. https://doi.org/10.5194/nhess-21-1667-2021

Mori N, Takahashi T, the 2011 Tohoku earthquake tsunami joint survey group (2012) Nationwide post event survey and analysis of the 2011 Tohoku earthquake tsunami. Coast Eng J 54:1250001-1–1250001-27. https://doi.org/10.1142/S0578563412500015

Morton RA, Gelfenbaum G, Jaffe BE (2007) Physical criteria for distinguishing sandy tsunami and storm deposits using modern examples. Sediment Geol 200:184–207. https://doi.org/10.1016/j.sedgeo.2007.01.003

Nakanishi R, Okamura S (2019) Tsunami deposits from the 1640 Hokkaido Komagatake eruption, north Japan: constraints on inundation heights and numerical simulation of volcanic debris avalanche-derived tsunami. J Geol Soc Jpn 125:835–851 (**in Japanese with English abstract**)

Nakanishi R, Ashi J, Miyairi Y, Yokoyama Y (2021) Spatial extension of the mid to late Holocene sedimentary record of tsunamis along the Southern Kuril Trench, Hokkaido Japan. Essoar. https://doi.org/10.1002/essoar.10508687.1

Nakanishi R, Ashi J, Miyairi Y, Yokoyama Y (2022) Holocene coastal evolution, past tsunamis, and extreme wave event reconstructions using sediment cores obtained from the central coast of Hidaka, Hokkaido. Jpn Mar Geol 443:106663. https://doi.org/10.1016/j.margeo.2021.106663

Nakanishi R, Okamura S, Yokoyama Y, Miyairi Y, Sagayama T, Ashi J (2020) Holocene tsunami, storm, and relative sea level records obtained from the southern Hidaka coast, Hokkaido. Jpn Quat Sci Rev 250:106678. https://doi.org/10.1016/j.quascirev.2020.106678

Nanayama F, Satake K, Furukawa R, Shimokawa K, Atwater BF, Shigeno K, Yamaki S (2003) Unusually large earthquakes inferred from tsunami deposits along the Kuril trench. Nature 424:660–663. https://doi.org/10.1038/nature01864

Namegaya Y, Satake K (2014) Reexamination of the A.D. 869 Jogan earthquake size from tsunami deposit distribution, simulated flow depth, and velocity. Geophys Res Lett 41:2297–2303. https://doi.org/10.1002/2013GL058678

Namegaya Y, Yata T (2014) Tsunami which affected the Pacific coast of eastern Japan in medieval times inferred from historical documents. J Seismol Soc Jpn 2nd Ser 66:73–81 (**in Japanese with English abstract**)

Nara FW, Yokoyama T, Yamasaki S, Minami M, Asahara Y, Watanabe T, Yamada K, Tsuchiya N, Yasuda Y (2021) Characteristics in trace elements compositions of tephras (B-Tm and To-a) for identification tools. Geochem J 5:117–133. https://doi.org/10.2343/geochemj.2.0619

Naruse H, Abe T (2017) Inverse tsunami flow modeling including nonequilibrium sediment transport, with application to deposits from the 2011 Tohoku-Oki tsunami. J Geophys Res Earth Surf 122:2159–2182. https://doi.org/10.1002/2017JF004226

Nishimura Y, Miyaji N (1998) On height distribution of tsunami caused by the 1640 eruption of Hokkaido-Komagatake, northern Japan. Bull Volcanol Soc Jpn 43:239–242 (**in Japanese**)

Okuno J, Nakada M, Ishii M, Miura H (2014) Vertical tectonic crustal movements along the Japanese coastlines inferred from late Quaternary and recent relative sea-level changes. Quat Sci Rev 91:42–61. https://doi.org/10.1016/j.quascirev.2014.03.010

Oppenheimer C, Wacker L, Xu J, Galván JD, Stoffel M, Guillet S, Corona C, Sigl M, Di Cosmo N, Hajdas I, Pan B, Breuker R, Schneider L, Esper J, Fei J, Hammond JOS, Büntgen U (2017) Multi-proxy dating the 'Millennium Eruption' of Changbaishan to late 946 CE. Quat Sci Rev 158:164–171. https://doi.org/10.1016/j.quascirev.2016.12.024

Reimer PJ, Austin WEN, Bard E, Bayliss A, Blackwell PG, Bronk Ramsey C, Butzin M, Cheng H, Edwards RL, Friedrich M, Grootes PM, Guilderson TP, Hajdas I, Heaton TJ, Hogg AG, Hughen KA, Kromer B, Manning SW, Muscheler R, Palmer JG, Pearson C, 21 van der Plicht J, Reimer RW, Richards DA, Scott EM, Southon JR, Turney CSM, Wacker L, Adolphi F, Büntgen U et al (2020) The IntCal20 Northern Hemisphere Radiocarbon Age Calibration Curve (0–55 cal kBP). Radiocarbon 62:725–757. https://doi.org/10.1017/RDC.2020.41

Satake K (2007) Volcanic origin of the 1741 Oshima-Oshima tsunami in the Japan Sea. Earth Planets Space 59:381–390. https://doi.org/10.1186/BF03352698

Satake K, Nanayama F, Yamaki S (2008) Fault models of unusual tsunami in the 17th century along the Kuril trench. Earth Planets Space 60:925–935. https://doi.org/10.1186/BF03352848

Sato K, Yamada M, Ishimura D, Ishizawa T, Bata T (in press) Numerical estimation of a tsunami source at the flexural area of Kuril and Japan Trenches in the 15th–17th century based on paleotsunami deposit distributions in northern Japan. Prog Earth Planet Sci.

Sawai Y (2020) Subduction zone paleoseismology along the Pacific coast of northeast Japan—progress and remaining problems. Earth Sci Rev 208:103261. https://doi.org/10.1016/j.earscirev.2020.103261

Sawai Y, Kamataki T, Shishikura M, Nasu H, Okamura Y, Satake K, Thomson KH, Matsumoto D, Fujii Y, Komatsubara J, Aung TT (2009) Aperiodic recurrence of geologically recorded tsunamis during the past 5500 years in eastern Hokkaido. Jpn J Geophys Res Solid Earth. https://doi.org/10.1029/2007JB005503

Sawai Y, Namegaya Y, Okamura Y, Satake K, Shishikura M (2012) Challenges of anticipating the 2011 Tohoku earthquake and tsunami using coastal geology. Geophys Res Lett 39:1–6. https://doi.org/10.1029/2012GL053692

Sugawara D (2021) Numerical modeling of tsunami: advances and future challenges after the 2011 Tohoku earthquake and tsunami. Earth Sci Rev 214:103498. https://doi.org/10.1016/j.earscirev.2020.103498

Suzuki T, Kasahara A, Nishizawa F, Saito H (2014) Chemical characterization of volcanic glass shards by energy dispersive X-ray spectrometry with EDAX Genesis APEX2 and JEOL JSM-6390. Geogr Rep Tokyo Metropolitan Univ. 49: 1–12.

Takada K, Nakata T, Miyagi T, Haraguchi T, Nishitani Y (2002) Handy geoslicer—new soil sampler for quaternary geologist. Chishitsu News 579:12–18 (**in Japanese**)

Takada K, Shishikura M, Imai K, Ebina Y, Goto K, Koshiya S, Yamamoto H, Igarashi A, Ichihara T, Kinoshita H, Ikeda T, Iwate Prefecture Government River Division Department of prefectural Land Development (2016) Distribution and ages of tsunami deposits along the Pacific Coast of the Iwate Prefecture. Act Fault Paleoearthq Res Rep Geol Surv Jpn 16:1–52 (**in Japanese with English abstract**)

Takashimizu Y (2014) Review of previous studies on tsunami deposits in Hokkaido, northern Japan: focusing on the studies of deposits from 17th century large tsunamis and others. J Geol Soc Jpn 119:599–612 (**in Japanese with English abstract**)

Takashimizu Y, Sagayama T, Nishina K, Oka T, Nakamura Y, Nishimura Y (2007) A 17th-century tsunami deposits discovered on the eastern Iburi Coast, Hokkaido, northern Japan. Quat Res 46:119–130 (**in Japanese with English abstract**)

Tanigawa K, Sawai Y, Shishikura M, Namegaya Y, Matsumoto D (2014) Geological evidence for an unusually large tsunami on the Pacific coast of Aomori, northern Japan. J Quat Sci 29:200–208. https://doi.org/10.1002/jqs.2690

Tanioka Y, Nishimura Y, Hirakawa K, Imamura F, Abe I, Abe Y, Shindou K, Matsutomi H, Takahashi T, Imai K, Harada K, Namegawa Y, Hasegawa Y, Hayashi Y, Nanayama F, Kamataki T, Kawata Y, Fukasawa Y, Koshimura S, Hada Y, Azumai Y, Hirata K, Kamikawa A, Yoshikawa A, Shiga T, Kobayashi M, Masaka S (2004) Tsunami run-up heights of the 2003 Tokachi-oki earthquake. Earth Planets Space 56:359–365. https://doi.org/10.1186/BF03353065

Tetsuka H, Goto K, Ebina Y et al (2020) Historical and geological evidence for the seventeenth-century tsunamis along Kuril and Japan trenches: implications for the origin of the AD 1611 Keicho earthquake and tsunami, and for the probable future risk potential. Geol Soc London Spec Publ. https://doi.org/10.1144/sp501-2019-60

Tsuji Y, Mabuchi Y, Okada K, Kuroyanagi Y, Kinami T, Matsuoka Y, Sato M, Haga Y, Imamura F (2014) Height distributions of the tsunamis accompanied with the 1677 North Sanriku-oki, the 1763 Hachinohe-oki, and the 1856 North Sanriku-oki earthquakes on the coast of the north part of Tohoku district. Rep Tsunami Eng 31:149–199 (**in Japanese**)

Tsushima K, Takizawa F (1977) Geology of the Shiriyazaki district. Geological Survey of Japan

Utsu T (2004) Catalog of damaging earthquakes in the world (through 2002), Tokyo. http://iisee.kenken.go.jp/utsu/index_eng.html. Accessed 11 Apr 2022

Velasco-Reyes ER, Goto K, Sugawara D, Nishimura Y, Shinohara T, Chiba T (2022) Paleotsunami history of Hachinohe, northern Japan: a multiproxy analysis and numerical modeling approach. Prog Earth Planet Sci 9:19. https://doi.org/10.1186/s40645-022-00477-4

Watanabe H (1998) Comprehensive list of tsunamis to hit the Japanese Islands, 2nd edn. University of Tokyo Press, Tokyo (**in Japanese**)

## Publisher's Note

Springer Nature remains neutral with regard to jurisdictional claims in published maps and institutional affiliations.